Darmstadt University of Applied Sciences

Faculty of Mathematics and Natural Sciences
Faculty of Computer Science

Machine Learning-based Regularization for Magnetic Particle Imaging

Submitted in partial fulfilment of the requirements for the degree of

Master of Science (M.Sc.)

by

Corinna Erika Rentschler

Matriculation number: 769282

Supervisor	:	Prof. Dr. Andreas Weinmann
Co-Supervisor	:	Prof. Dr. Elke Hergenröther
Date of registration	:	December 5, 2022
Date of submission	:	May 12, 2023

DECLARATION

Ich versichere hiermit, dass ich die vorliegende Arbeit selbstständig verfasst und keine anderen als die im Literaturverzeichnis angegebenen Quellen benutzt habe.

Alle Stellen, die wörtlich oder sinngemäß aus veröffentlichten oder noch nicht veröffentlichten Quellen entnommen sind, sind als solche kenntlich gemacht.

Die Zeichnungen oder Abbildungen in dieser Arbeit sind von mir selbst erstellt worden oder mit einem entsprechenden Quellennachweis versehen.

Diese Arbeit ist in gleicher oder ähnlicher Form noch bei keiner anderen Prüfungsbehörde eingereicht worden.

Darmstadt, den 12. Mai 2023

Corinna Erika Rentschler

ABSTRACT

Magnetic Particle Imaging (MPI) is an emerging medical imaging modality which aims to reconstruct a particle concentration from measured voltage. In order to acquire scan data, the nonlinear response of superparamagnetic iron oxide nanoparticles (SPIO) to external magnetic fields is exploited. The modality is tracer based and inherits advantageous properties like high sensitivity, temporal and spatial resolution while working without radioactive materials or X-Rays. For that reason, many applications in the medical field could benefit from MPI.

In this work, the measurement-based approach using a lengthy calibration process in order to acquire the system response at each voxel position is applied. Consequently, the relation between concentration distribution and measured voltage can be described as a system of linear equations. Since the problem is ill-posed, regularization techniques are used to reconstruct the concentration distribution. The goal of this thesis is to implement and compare one standard and two different Machine Learning-based regularization techniques to approach the inverse problem and reconstruct MPI data from a preclinical scanner.

In order to reconstruct the data, three regularization techniques are applied: Besides L^2-Tikhonov Regularization, Machine Learning-based methods Deep Image Prior (DIP) and Plug and Play Prior (PnP) are implemented in Python. To denoise reconstructed volumes within the PnP framework, a pretrained denoiser Convolutional Neural Network (CNN) is used. Preprocessing of the data is described and implemented in Matlab. The results of reconstructed concentration distributions by the implemented different regularization techniques are evaluated by the standard image quality measures SSIM and PSNR.

The results differ by the scanned phantom and preprocessing applied to the data. Regarding SSIM, L^2-Tikhonov Regularization recoonstructs in most cases the best results using preprocessed data of a phantom consisting of thin tubes. It is shown that Learning-based techniques lead to a better image quality of a phantom with a large area: Edges are preserved while the noise level is low. This applies to both the visual impression and image quality measures. The tuning of hyperparameters is non-trivial and crucial for the image quality. Both Learning-based methods require early stopping of the training process. The best visual result of a phantom with a large amount of low frequent parts is achieved in the first iteration of the PnP.

Keywords: Magnetic Particle Imaging, Machine Learning, Medical Imaging, Algorithms, Regularization, Data Science

ZUSAMMENFASSUNG

Magnetic Particle Imaging (MPI) ist eine neuartige medizinische Bildgebungsmodalität, bei der die Konzentration paramagnetischer Partikel anhand gemessener Spannung rekonstruiert wird. Dabei wird die nichtlineare Antwort superparamagnetischer Eisenoxid Nanopartikel (SPIO) auf externe Magnetfelder für die Signalerhebung von MPI ausgenutzt. Die Modalität ist tracerbasiert und bietet vorteilhafte Eigenschaften wie hohe Sensitivität und hohe zeitliche sowie örtliche Auflösung. Dabei verzichtet MPI auf radioaktive oder Röntgenstrahlung. Daher könnten viele Anwendungen in der Medizin von MPI profitieren.
Der messbasierte Ansatz für MPI wird in dieser Arbeit verfolgt. Dabei wird während eines zeitintensiven Kalibrationsprozesses die Systemantwort eines Scanners bei jeder Voxelposition erfasst. Folgend wird der Zusammenhang zwischen Konzentrationsverteilung und gemessener Spannung als lineares Gleichungssystem beschrieben. Dieses Problem ist schlecht gestellt, weswegen Regularisierungstechniken zur Rekonstruktion eingesetzt werden. Ziel dieser Thesis sind Implementierung und der Vergleich verschiedener Machine Learning-basierten Regularisierungstechniken und einem Standardregularisierungsverfahren um das inverse Problem anzugehen und MPI Daten eines preklinischen Scanners zu rekonstruieren.
Neben einer L^2-Tikhonov Regularisierung werden Machine Learning-basierte Methoden Deep Image Prior (DIP) und Plug and Play Prior (PnP) implementiert. Um die rekonstruierten Volumina mit PnP zu entrauschen, wurde ein vortrainiertes entrauschendes künstliches neuronales Faltnetz (CNN) verwendet. Die Datenvorverarbeitung wird beschrieben und in Matlab implementiert. Die Bildqualität der Resultate wird anhand Standardbildqualitätsmaße SSIM und PSNR quantifiziert.
Die Ergebnisse unterscheiden sich anhand der gescannten Phantome und Datenvorverarbeitung. Gemessen an SSIM führt die L^2-Tikhonov Regularisierung von Daten eines Phantoms bestehend aus dünnen Stäben meistens zu den besten Ergebnissen. Es wird gezeigt, dass die implementierten lernbasierten Techniken zu besserer Bildqualität eines Phantoms mit großen Flächen führt. Dabei werden Kanten bei niedrigem Rauschlevel erhalten, was sowohl der visuelle Eindruck, als auch Bildqualitätsmaße zeigen. Hyperparametertuning ist nicht trivial und entscheidend für die resultierende Bildqualität. Frühzeitiges Abbrechen ist bei beiden lernbasierten, iterativen Techniken notwendig. Das beste visuelle Ergebnis des flächigen Phantoms wurde in der ersten Iteration von PnP erreicht.

Keywords: Magnetic Particle Imaging, Maschinelles Lernen, Medizinische Bildgebung, Algorithmen, Regularisierung, Data Science

CONTENTS

1 Introduction 1
1.1 Motivation . . . 1
1.2 Goal of this thesis . . . 2
1.3 Structure of this thesis . . . 2
2 Background and state of research 3
2.1 MPI principle . . . 3
2.1.1 Superparamagnetic Iron Oxide (Nanoparticles) (SPIO) . 3
2.1.2 Technical implementaion: Selection Field, Drive Field and Field Free Point . . . 4
2.1.3 Measurement-based approach to MPI reconstruction . . 6
2.1.4 Possible clinical applications and comparison to other medical imaging modalities . . . 10
2.2 Open MPI Data . . . 11
2.2.1 MPI scanner (Bruker) . . . 11
2.2.2 Scan Sequences . . . 12
2.2.3 Calibration . . . 14
2.2.4 Phantoms . . . 14
3 Methods 16
3.1 Data preprocessing . . . 16
3.2 Reconstruction and Regularization Techniques . . . 20
3.2.1 Ill-posed problems . . . 20
3.2.2 Tikhonov regularization . . . 21
3.2.3 Learning-based techniques . . . 22
3.3 Image Quality Measures . . . 28
3.3.1 Peak Signal to Noise Ratio (PSNR) . . . 28
3.3.2 Structural Similarity Index Measure (SSIM) . . . 29
4 Results 30
4.1 References . . . 30
4.2 Tikhonov Regularization . . . 31
4.3 Deep Image Prior (DIP) . . . 35
4.4 Plug and Play Prior (PnP) . . . 43
4.4.1 Choice of the axis along which the reconstructed volume is sliced . . . 43
4.4.2 Hyperparameters . . . 43
4.5 Comparison of the different results . . . 48
5 Discussion 50
5.1 Data and Preprocessing . . . 50
5.2 Tikhonov Regularization . . . 51
5.3 DIP . . . 51
5.4 PnP . . . 52
5.5 Outlook . . . 53
6 Conclusion 54

A Appendix 56
A.1 Hyperparameters of the regularization techniques leading to highest Image Quality Measures 56

Bibliography 58

LIST OF FIGURES

Figure 2.1 Magnetization of a paramagnetic substance. 4
Figure 2.2 Magnetization response of unsaturated paramagnetic particles 5
Figure 2.3 Magnetization response of saturated paramagnetic particles 6
Figure 2.4 Superposition of Drive field and Selection Field. 6
Figure 2.5 Schematic MPI scanner setup. 7
Figure 2.6 Imaging of a mouse with two probes of SPIO tracer. . . 10
Figure 2.7 Comparison of MPI with other medical imaging modalities 11
Figure 2.8 Preclinical MPI scanner used for data acquisiton of the OpenMPIData initiative. 12
Figure 2.9 Sampling points of the FFP during one period of the 2D Scan Sequence. 13
Figure 2.10 Phantoms used in the open MPI datasets. 15
Figure 3.1 Preprocessing steps applied to MPI data. 16
Figure 3.2 Frequency analysis of receive coil 1 of the real part of Fourier transformed background measurements from the shape phantom scanned with a 3D sequence. 17
Figure 3.3 Singular value decay of a normalized and background corrected System Matrix 20
Figure 3.4 Comparison of "traditional" deep learning techniques vs. the Deep Image Prior method. 22
Figure 3.5 Architecture of the deep CNN DRUnet denoiser prior. In addition to an input image, the net takes a Noise Level Map in order to receive a Denoised Image. Strided convolution "Sconv" and transposed convolution "Tconv" blocks are used. [Zha+] 26
Figure 3.6 Denoising along a randomly chosen axis. 27
Figure 4.1 References of the two phantoms used, sliced in each axis. 30
Figure 4.2 Image quality measures of Tikhonov Regularization Results with different penalty parameter α. 32
Figure 4.3 Best results of the L^2 regularization according to PSNR_{max} and SSIM_{max} values. 33
Figure 4.4 Reconstruction of the Shape phantom with Tikhonov L^2-regularization using not suitable penalty strength. . 34
Figure 4.5 Image quality measures PSNR_{max} and SSIM_{max} of the DIP result using different seeds. 35
Figure 4.6 Comparison of the reconstruction of the Shape phantom using the DIP method and different seeds. 36

Figure 4.7 Image quality measures $PSNR_{max}$ and $SSIM_{max}$ of DIP results over learning iterations using different preprocessed data. . . . 38
Figure 4.8 Image quality measure $SSIM_{max}$ of different preprocessed data using DIP split according to the step size used. . . . 39
Figure 4.9 Image quality measures $PSNR_{max}$ and $SSIM_{max}$ over a large number of iterations. . . . 40
Figure 4.10 DIP result of the Shape phantom, with step size 10^{-3} after different iterations. . . . 41
Figure 4.11 DIP result of the Shape phantom, with step size 10^{-3} after different iterations. . . . 42
Figure 4.12 $PSNR_{max}$ and $SSIM_{max}$ of the PnP approach using different slicing methods. . . . 44
Figure 4.13 Shape phantom reconstructions of PnP applying random vs. set chosen slicing axis. . . . 44
Figure 4.14 $PSNR_{max}$ and $SSIM_{max}$ of Resolution phantom reconstructions using PnP. . . . 45
Figure 4.15 Reconstruction of Resolution phantom data at different iterations of the PnP method. . . . 46
Figure 4.16 $PSNR_{max}$ and $SSIM_{max}$ of Shape phantom data reconstructions at different PnP iterations. . . . 46
Figure 4.17 Example of high image quality after the first iteration of the PnP result vs. low image quality after 40 iterations 47

LIST OF TABLES

Table 2.1 Overview of Scan Sequence Parameters. 13

Table 4.1 Best image quality measures of the Shape phantom reconstruction using different Regularization techniques split according to SNR-filtering with threshold τ during preprocessing. Data were preprocessed without Normalization. The highest values of each preprocessed data set are underlined. 48

Table 4.2 Best image quality measures of the Shape Phantom reconstruction using different Regularization techniques split according to SNR-filtering with threshold τ during preprocessing. Data were preprocessed with Normalization. The highest values of each preprocessed data set are underlined. 48

Table 4.3 Best image quality measures of the Resolution Phantom reconstruction using different Regularization techniques split according to SNR-filtering with threshold τ during preprocessing. Data were preprocessed without Normalization. The highest values of each preprocessed data set are underlined. 49

Table 4.4 Best image quality measures of the Resolution Phantom reconstruction using different Regularization techniques split according to SNR-filtering with threshold τ during preprocessing. Data were preprocessed with Normalization. The highest values of each preprocessed data set are underlined. 49

Table A.1 Regularization parameter α of L^2-Regularization leading to highest values of image quality measures. 56

Table A.2 Step size of the DIP method leading to highest values of image quality measures. 56

Table A.3 Number of iteration of the DIP method leading to highest values of image quality measures. 56

Table A.4 Hyperparameter α_{start} of the PnP method leading to highest values of image quality measures. 57

Table A.5 Hyperparameter α_{incr} of the PnP method leading to highest values of image quality measures. 57

Table A.6 Hyperparameter $\lambda\sigma^2$ of the PnP method leading to highest values of image quality measures. 57

LIST OF ACRONYMS

ADMM Alternating Direction Method of Multipliers

CG Conjugate Gradient

cMPI color Magnetic Particle Imaging

CNN Convolutional Neural Network

CT Computed Tomography

DIP Deep Image Prior

FOV Field of View

FFL Field Free Line

FFP Field Free Point

HQS Half Quadratic Splitting method

LASSO Least Absolute Shrinkage and Selection Operator

MAP Maximum A Posteriori

MDF Magnetic Particle Imaging Data Format

MPI Magnetic Particle Imaging

MRA Magnetic Resonance Angiogram

MRI Magnetic Resonance Imaging

MSE Mean Squared Error

OLS Ordinary Least Squares

PET Positron Emission Tomography

PnP Plug and Play Prior

PSNR Peak Signal to Noise Ratio

SM System Matrix

SPIO Superparamagnetic Iron Oxide (Nanoparticles)

SSIM Structural Similarity Index Measure

TV Total Variation

1 INTRODUCTION

1.1 MOTIVATION

Magnetic Particle Imaging (MPI) is an emerging imaging modality which exploits the nonlinear magnetization of Superparamagnetic Iron Oxide (Nanoparticles) (SPIO) in order to reconstruct the particle distribution in a scanned volume. The goal is to recover the spatial distribution of SPIO from a time dependent voltage signal that is measured by MPI. Having been introduced by Gleich and Weizenecker [GW05] in 2005, MPI has been further developed as it promises high potential in medical imaging: It offers high spatial resolution, high temporal resolution and sensitivity [Wu+19]. Furthermore, neither X-Ray like in Computed Tomography (CT) nor radioactive tracers as in Positron Emission Tomography (PET) are used which offers an advantage for patients [Wu+19]. As an example in the medical field, a tracer containing SPIOs can be injected into the patient's circulatory system and thus show the concentration of the tracer and consequently, gaining information of flow properties and detecting stenosis. A further possible application is the diagnostics of cancer cells [Häg+12]. There are promising results that indicate future applications in medical imaging, overcoming the challenging engineering task to create a strong gradient field in order to achieve a scanner big enough to scan a human brain [Le+23].
As a result of a time-consuming calibration process, the MPI problem can be described as a linear system of equations that has to be inverted. Here, the system matrix S consisting of the discretized system answer multiplied with the unknown concentration vector c on the left hand side, should equal the measured voltage (vector) u on the right hand side of the equation leading to the system of linear equations $Sc = u$. However, MPI suffers from ill-posedness [KJL18], which leads to the need of regularization techniques in order to receive a stable solution. Moreover, conditions related to the problem like the existence of only positive particle concentrations or the assumption of sparse distributed concentration can be taken in account and implemented by considering suitable priors in regularization techniques.
This thesis focuses on applying different regularization techniques in order to deal with the MPI problem. The goal is to reconstruct the volume of SPIO concentration distribution from MPI data. A standard Tikhonov regularization and two learning-based methods are investigated and implemented. Furthermore, the influence of different preprocessing steps is analyzed.
Image quality of the results is quantified by Structural Similarity Index Measure (SSIM) and Peak Signal to Noise Ratio (PSNR).

1.2 GOAL OF THIS THESIS

The goal of this thesis is to understand and preprocess freely accessible MPI data of a reals scanner and perform reconstruction with Machine learning-based regularization techniques. The reconstruction of the data is approached in a measurement-based way. Furthermore, different regularization techniques are implemented, tuned and the results evaluated by standard image quality measures.
As a baseline, Tikhonov regularization is implemented. Moreover, Machine learning-based techniques are also implemented and their results regarding image quality evaluated. The few amount of freely accessible MPI data challenges the application of learning-based methods and has to be taken into account during the finding process of suitable Machine learning-based regularization techniques.
An objective is to provide inside into the strengths and weaknesses of different regularization techniques applied to acutal scan data.

1.3 STRUCTURE OF THIS THESIS

First, Background information needed to understand the functionality of MPI and the measurement-based approach is provided. The signal generation from particles with certain properties, technical implementation and spatial encoding is described. Afterwards, the measurement based approach to MPI construction is explained since this is the core operation used in this thesis to reconstruct MPI data. To complete the understanding of MPI, possible clinical applications of MPI are stated.
Then, freely accessible MPI data including the used MPI scanner, scan sequences, calibration procedure and scanned phantoms are introduced and described. Methods applied for the calculation of the MPI reconstruction in this thesis are introduced in Chapter 3. This includes different steps of preprocessing of the freely accessible data. Preprocessing is used to exclude background and also augments the few data. Afterwards, the notion of ill-posedness is introduced in order to motivate the usage of regularization techniques. Then, Tikhonov regularization and the Machine learning-based regularization methods Deep Image Prior and the Plug and Play framework with a convolutional neural network as denoiser are explained. Since the resulting image quality has to be quantified, image quality measures are introduced.
The results of regularization techniques including tuned hyperparameters are provided and evaluated by standard image quality measures in Chapter 4.
Having described the results, their further properties are discussed as well as challenges that might have an influence on the results.
Finally, the main findings and challenges of the thesis are summarized.

2

BACKGROUND AND STATE OF RESEARCH

This chapter deals with the functionality of Magnetic Particle Imaging. First, the functionality of Magnetic Particle Imaging (MPI) and the measurement-based approach to MPI is described. Afterwards, the dataset used in this thesis is introduced.

2.1 MPI PRINCIPLE

In this section, the technical functionality of MPI is explained, starting from the used Superparamagnetic Iron Oxide tracers, their response to external applied magnetic fields and measurement of the resulting signal. Moreover, the superimposition of different magnetic fields in order to excite SPIOs and provide local encoding is described. Followingly, the measurement-based approach to MPI is shown so that the usage of the SM, which is the main component of the measurement-based approach to MPI, is understood. Finally, possible clinical applications for MPI are explained and the difference to other medical imaging modalities is summarized.

2.1.1 *Superparamagnetic Iron Oxide (Nanoparticles) (SPIO)*

Magnetic Particle Imaging exploits the nonlinear magnetization respronse of Superparamagnetic Iron Oxide Nanoparticles [GW05] exposed to magnetic fields. This chapter introduces the properties of SPIO and the advantages for medical imaging.
Paramagnetism refers to the property of particles to be strongly magnetized in a magnetic field and in contrast to ferromagnetism, no magnetization is retained after switching off the magnetic field. Thus no magnetic remanence is formed when a previously applied magnetic field has been turned off as shown in Figure 2.1. If this property remains even below the Curie temperature, it is described as superparamagnetism. This effect occurs below a substance-dependant size of ferromagnetic or ferrimagnetic material [TSH03]. Superparamagnetic iron oxide nanoparticles (SPIO) consist of an iron oxide core which is surrounded by a non-ferrous shell [Bie12]. The diameter of the core ranges between 10nm and 100nm [WA12]. In MPI, the nonlinear magnetization of SPIO is used for imaging.
SPIO as contrast agent is already used in the field of medical imaging, more precisely it has found application in Magnetic Resonance Imaging (MRI) [TSH03] as well as drug carrier [WA12]. Conventional contrast media like gadolinium in MRI have been shown to be difficult to tolerate for some patient groups and, in severe cases, may even lead to increased mortality [Sar+13]. Since gadolinium is processed in the kidney, imaging with such

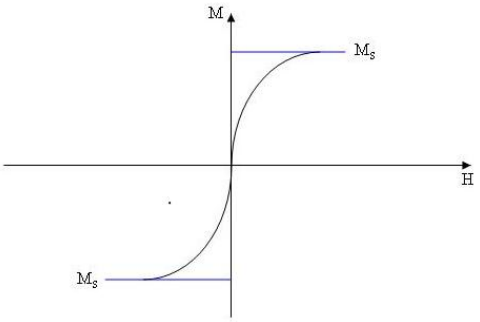

Figure 2.1: *Magnetization of a paramagnetic substance.* When a magnetic field H is applied, the absolute value of magnetization M increases until saturated at magnetization M_s. After switching off or without a magnetic field, the magnetization is 0. Source: https://commons.wikimedia.org/wiki/File:Hysteresis_superparamag.JPG

contrast media can be especially harmful for patients with chronic kidney disease. SPIO as contrast agent is safer for the patient than gadolinium due to the processing in the liver rather than in the kidneys [Sar+13].
However, SPIO appear dark in Magnetic Resonance Imaging, which leads to a negative contrast. This causes challenges and limitations in applications like the quantification of lumen area or the precise location of SPIO [Sar+13]. In opposition to that, SPIO in MPI are represented as "bright blood" contrast [Sar+13].

2.1.2 *Technical implementaion: Selection Field, Drive Field and Field Free Point*

To acquire the MPI scan signal, SPIO are excited with an alternating magnetic field, usually sinusoidal, of amplitude A^D and frequency f_0. If the dynamic drive field $H^D(x,t)$ with sufficiently high amplitude A^D is applied, a magnetization $M(t)$ is exhibited by the SPIO [GW05]. An example for the 1-dimensional case is shown in Fig. 2.2. Due to the sensitivity profile of the drive field coils, the resulting magnetic field varies along the spatial component x [MW]. The induced voltage in a receive coil shows dirac-like peaks (Fig. 2.2, top right). Since the magnetization curve of the particles does not follow a perfectly steep step function, the spectrum of the received voltage time-signal inherits harmonics of the excitation frequency f_0 [Kno11].
However, the drive field alone does not provide any spatial encoding since all particles in a volume respond to the excitation. For that reason, a static gradient field, selection field $H^s(x) = Gx$ with a linear gradient G is superimposed:

$$H(x,t) = H^S(x) + H^D(x,t) \ . \tag{2.1}$$

In a certain region, $H^s(x)$ is by design 0 [Kno11]. Using permanent magnets and/or coils in Maxwell configuration, the gradient field is generated [MW]. An overview of the coils used for a MPI scanner is found in Figure 2.5.
The magnetization of particles located in a saturated area are hardly influ-

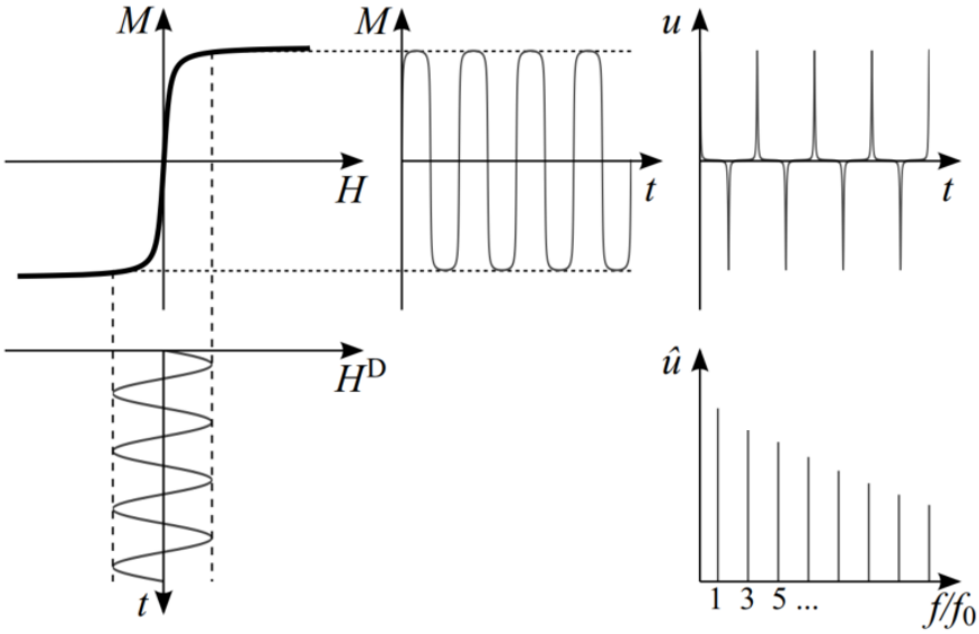

Figure 2.2: *Magnetization response of unsaturated paramagnetic particles.* A dynamic magnetic field (bottom left) acting on paramagnetic particles in their non-linear magnetization range (top left), leads to a magnetization response (top middle). The change in magnetization induces in the receiving coil a signal (top right) whose Fourier spectrum is non-trivial (bottom right). Source: [Kno11]

enced by an external dynamic field, which is shown in Fig. 2.3. Therefore, induced voltage in receive coils is trivial and the resulting coefficients of the spectrum are close to zero.

Due to the superimposition of drive field and selection field, the location of the point where $H(x,t) = 0$, is moved. This point is called Field Free Point (FFP). The effect of the superimposition is visualized in Fig. 2.4.

Only particles located in and in very close proximity to the FFP can be excited and thus induce a non-trivial signal in receive coils. As a consequence, spatial encoding is achieved.

There are also MPI scanners using a Field Free Line (FFL) geometry [WGB08] [TG20], which will not be discussed in the course of this thesis. All data processed in this study was acquired by a scanner with FFP geometry.

According to (2.1), the induced voltage in the receive coils results not only from the particle's magnetization change but is also influenced by the drive field itself. Therefore, the frequencies used for reconstruction are usually higher than the drive field base frequency f_0.

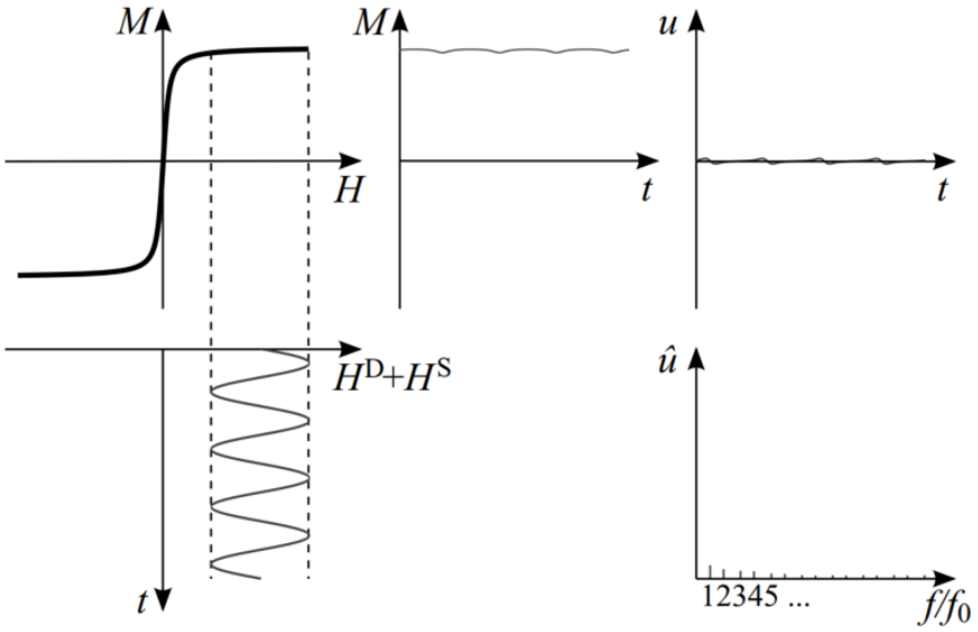

Figure 2.3: *Magnetization response of saturated paramagnetic particles.* A dynamic magnetic field (bottom left) acting on paramagnetic particles in a saturated range (top left), leads to a marginal change in their magnetization (top middle). Small changes of the magnetization induce very small voltages in the receive coil (top right). Followingly, the Fourier coefficients are close to 0 (bottom right). Source: [Kno11]

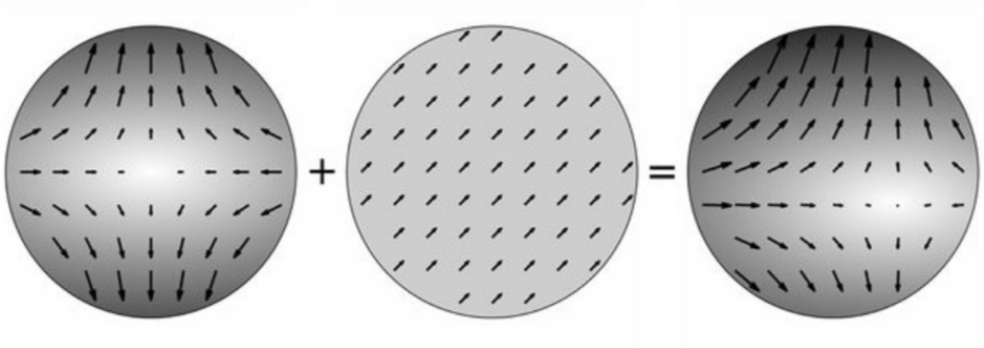

Figure 2.4: *Superposition of Drive field and Selection Field.* Superposition of a Drive field generating a Field Free Point (left) and gradient field (middle) leads to another position of the FFP (right). Source: Universität Bremen, Zentrum für Technomathematik, accessed 22.04.2023

2.1.3 *Measurement-based approach to MPI reconstruction*

Having measured the induced voltage signal with the receive coils, the goal of MPI is to reconstruct the particle concentration distribution of the scanned volume.
There are two different approaches to address the MPI reconstruction: Measurement-based and model-based. Both aim to derive information of the spatial concentration distribution from measured voltage signal.
In the following section, the measurement-based approach is described since

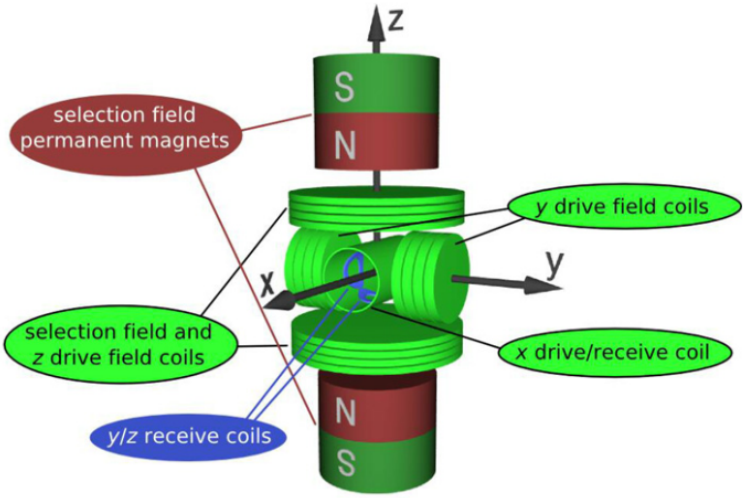

Figure 2.5: *Schematic MPI scanner setup.* Source: [Wei+09]

all of the following analysis and implementation is based on it. It should be noted that this approach inherits some drawbacks like a lengthy calibration process limitations of voxel grid size. In the model-based approach, the calibration process is avoided. For further information on the model-based approach, please refer to [Kno+10b; Kno+10a; MW].
The main goal is the reconstruction of the spatial particle concentration ρ from measured time signal $u(t)$ [MW].
The signal detected in a receive coil is induced voltage $u(t)$ by a temporal change of the magnetic flux $\Phi(t)$ according to Faraday's law of induction:.

$$u(t) = -\frac{d}{dt}\Phi(t) \quad . \tag{2.2}$$

In MPI, magnetic flux is the superposition of an applied magnetic field $H(x,t)$ and the magnetization response $M(x,t)$ of the SPIO in a volume $\Omega \in \mathbb{R}^3$:

$$\Phi(t) = \mu_0 \int_\Omega R(x)(H(x,t) + M(x,t))dx \quad . \tag{2.3}$$

Parameter μ_0 represents the magnetic permeability and $R(x) \in \mathbb{R}^{3x3}$ the sensitivity pattern of the three recording coil pairs [MW].
The magnetization response depends on the particle concentration ρ and magnetic moment m of a single particle which is influenced by the magnetic field:

$$M(x,t) = \rho(x)\, m(x,t) \tag{2.4}$$

The influence of a magnetic field on the magnetic moment is described by the Langevin function, which is visualized in Fig. 2.1. Hence, the induced voltage can be split into a particle concentration dependent part described by the magnetization response and a particle concentration independent part of the applied magnetic field (2.5). Since the latter one does not provide

information about the concentration distribution and thus is not of interest in terms of the MPI inverse problem, it is defined as background signal $b(t)$.

$$\begin{aligned} u(t) &= -\frac{d}{dt}\mu_0 \int_\Omega R(x)(M(x,t) + H(x,t))dx \\ &= -\mu_0 \frac{d}{dt} \int_\Omega R(x)M(x,t)dx \underbrace{-\frac{d}{dt}\mu_0 \int_\Omega R(x)H(x,t)dx}_{b(t)} \\ &= \int_\Omega \rho(x) \underbrace{(-\mu_0)R(x)\dot{m}(x,t)}_{s(x,t)} dx + b(t) \\ &= \int_\Omega \rho(x)s(x,t)dx + b(t) \end{aligned} \tag{2.5}$$

Parts of the background signal is filtered by analog filters in the signal acquisition chain. To eliminate the entire background signal from the induced voltage, the remaining background signal is estimated via measurements of an empty MPI scanner [KJ19].
The system answer $s(x,t)$ of one single magnetic particle consists of the material properties of the scanner and magnetic particle.
In reality, the background signal and particle signal is superimposed in the measured signal. To extract the signal induced by the magnetization response, measured signal is subtracted by measurements of an empty MPI scanner.
After the data acquisition, a discrete Fourier transformation is performed on the received voltage signal $u(t)$, leading to $K \in \mathbb{N}$ Fourier coefficients. Let $I_k = 1, 2, ...K$ and $k \in I_k$, then the k-th background-corrected Fourier coefficient $\hat{u}_k$ can be then described with Fourier coefficients $\hat{s}_k$ of $s(x,t)$:

$$\hat{u}_k = \int_\Omega \hat{s}_k(x)\rho(x)dx \tag{2.6}$$

By dispersing volume Ω into N discrete voxels of the same size, a discretized formula is obtained, where c_n is the SPIO concentration in voxel V_n, $n \in I_N$ with $I_N = 1, 2, ..., N$:

$$\hat{u}_k = \sum_{n=1}^{N} \hat{s}_{k,n} c_n \tag{2.7}$$

In matrix notation it becomes clear that the MPI problem can be adressed as a linear problem, if the System Matrix S is known:

$$\hat{u} = Sc \ . \tag{2.8}$$

The System Matrix (SM) is the discretized system function which can be obtained via a calibration process. During the calibration, the system response is measured by scanning a voxel-sized phantom "Delta Sample" of a known concentration at each voxel position. A detailed description of the calibration process is provided in section 2.2.3.
The columns of the System Matrix define the spatial position of the "Delta

Sample" during the calibration, therefore representing the voxel position in the volume to be reconstructed, which is also known as Field of View (FOV). The rows represent selected Fourier coefficients obtained by the Fourier Transformation of the calibration measurements. Each of the used L receive coils provides measurement data that can be added as rows to the System Matrix. Furthermore, the Fourier coefficients can be split into their real and imaginary part, which leads to a SM $S \in \mathbb{R}^{mxN}$, with m being the total number of Fourier coefficients used for the reconstruction. The number of suitable Fourier coefficients of the individual receive coil can vary. A selection of coefficients can be made by criteria, for instance bandpass filtering or signal to noise ratio. Let I_l be the set of Foursystem mier coefficients of receive channel l taken into account for the reconstruction. Then the number of rows m of the SM is: $m = 2 \cdot \sum_{l=1}^{L} |I_l|$.
The left hand side of (2.8) consists of vector $\hat{u} \in \mathbb{R}^m$, the elements are the corresponding Fourier coefficients of the voltage signal used for reconstruction.
Finally, the unknown particle concentration $c := (c_n)_{n \in I_N} \in \mathbb{R}_+^N$ can be obtained by solving the inverse problem associated to (2.7).
However, the reconstruction problem is severely ill-posed [KJ19], meaning a solution via inversion of the SM would lead to unstable results. An anlaysis of MPI scan data in section 3.1 shows that the SM is ill-conditioned since the SM has a high condition number. Consequently, a small change in the measurement vector u can lead to major changes in the reconstructed concentration distribution. The singular value decay on MPI scan data is investigated in [KJ19]. Therefore, a regularized reconstruction method is needed. Furthermore, implausible results like negative concentrations could be part of the calculated solution. Constraints like positivity constraint can be integrated in the regularization process to ensure that the solution fulfills certain properties.

2.1.4 *Possible clinical applications and comparison to other medical imaging modalities*

The signal of excited and relaxed SPIO tracer is measured in MPI. This means that only externally added tracers with certain properties are visible in the image of MPI. Unlike CT or MRI, the overall structure of the scan object is not measured and thus not visible in the resulting MPI images. Two imaging modalities can be combined to provide further spatial information of the scanned object's structure [Vog+19]. An example is shown in Fig. 2.6, where the structural information provided by CT scans is visualized in grayscales and SPIO concentration measured with MPI is visualized using colors.
Tracer imaging is used in medical imaging modalities like PET. A disadvantage of these tracers is the radioactivity to which a patient is exposed. SPIO are not radioactive, which is a great advantage compared to PET.
Moreover, since SPIO are better tolerated compared to other contrast media used in MRI [Sar+13]. Clinical applications for MPI are the diagnosic

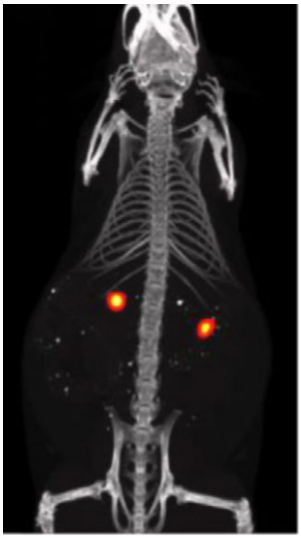

Figure 2.6: *Imaging of a mouse with two probes of SPIO tracer.* The grayscale structural imaging is from CT, color coded areas MPI reconstruction. Source: [Tal+20]

of tumors [Häg+12] and dynamic scans like myocardperfusion [Häg+12] or general scan of the flow through a blood vessel in order to detect stenosis.
An overview of MPI's properties compared to other medical imaging modalities is provided in Fig. 2.7. Main advantages are high sensitivity, high temporal resolution and depending on a calibration process or model-based approach, high spatial resolution [Wu+19].

Modality	Ultrasound	CT	MRI	PET	SPECT	MPI
Main clinical applications	Structural imaging	Structural imaging	Structural imaging	Tracer imaging	Tracer imaging	Tracer imaging
Spatial resolution	1 mm	<1 mm	1 mm	4 mm	3–10 mm	1 mm
Temporal resolution	<1 second	Seconds	Seconds to hours	Minutes	Minutes	<1 second to minutes
Contrast agents/tracers	Microbubbles	Iodine	Gadolinium, iron oxide particles	Radioactive tracers	Radioactive tracers	Iron oxide particles
Sensitivity	Low	Low	Low	High	High	High
Patient risk	Heating and cavitation	Radiation	Heating and peripheral nerve stimulation	Radiation	Radiation	Heating and peripheral nerve stimulation
Cost	Low	Medium	High	High	Medium	Medium

Figure 2.7: *Comparison of MPI with other medical imaging modalities.* Source: [Wu+19]

2.2 OPEN MPI DATA

In this thesis, public data of the Open MPI dataset [Kno+20] (downloaded from https://media.tuhh.de/ibi/openMPIData/, accessed on April 12, 2023) provided in the Magnetic Particle Imaging Data Format (MDF) [Kno+18] is used to investigate the application of different regularization techniques. Acquired by a preclinical MPI scanner (Bruker in Ettlingen, Germany) in February 2018, the data inherit all properties of a real scan setup including noise and technology-induced perturbations. In the following section, a closer investigation of the scanner, data acquisition process and scan phantoms is provided. Preprocessing steps needed to achieve a reasonable image quality are discussed in Chapter 3.1.

2.2.1 *MPI scanner (Bruker)*

The preclinical scanner as well as the corresponding coordinate system is shown in Fig. 2.8. It was developed by Bruker in cooperation with Royal Philips. The MPI scanner used to measure the Open MPI dataset was installed at the University Medical Center Hamburg-Eppendorf in 2014 [Kno+20]. The bore size is 11.9cm, which makes it accessible for phantoms and smaller laboratory animals like rats and mice. The maximum FOV of one image is limited to 10cm$\times$10cm. With a speed of up to 46 volumes per second, biological processes can be imaged in real time. According to Bruker's marketing brochures [Bru20] (downloaded from https://www.bruker.com/de/products-and-solutions/preclinical-imaging/mpi.html, accessed on April 12, 2023), this is 1000 times faster than imaging via PET.
The scanner uses a FFP geometry, whose trajectory is determined by a drive field of 3 dimensions with up to 12mT and frequency of 25kHz. Depending on the scan sequence, between one and three drive fields are used.

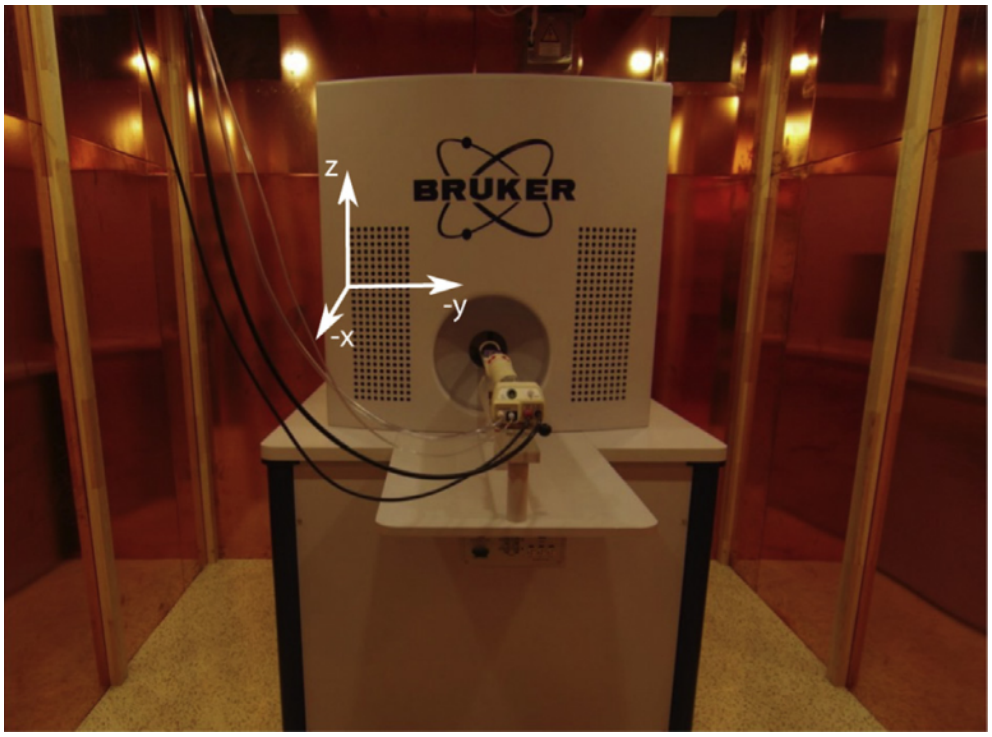

Figure 2.8: *Preclinical MPI scanner used for data acquisiton of the OpenMPIData initiative.* The corresponding coordinate system is shown in white. Source: [Kno+20]

2.2.2 *Scan Sequences*

Scan Sequences define the trajectory and velocity of the field free point. Consequently, a scan sequence controls the sampling of the scanned region and influences the temporal resolution of the result, especially if a movement of the object of interest is involved.
The Bruker scanner provides three different scan sequences: 1D, 2D and 3D. According to the naming, the sequence defines the sampling along a line, a plane or a volume. This is implemented by adding a dynamic field along the chosen number of dimension. For MPI, different types of trajectories have been tested. The preclinical scanner used to acquire the scan data uses a Lissajous-type trajectory. As a consequence, the field free point moves in a Lissajous-type trajectory (2.9). The sampling points of the FFP during one period of the 2D sequence is shown in Fig. 2.9.
In order to sample the whole volume using 1D or 2D sequence, the object is moved by a robot after each completed scan along the scan line or plane, accordingly. In case of a 2D sequence, the phantom is moved step-wise along the z-axis. One robot position thus represents one patch. One set of individual scans that describe the whole volume (FOV) is called one frame. An overview of the different parameters and scan sequences is found in table 2.1.
The Lissajous-type FFP trajectory controlled by the strength of magnetic field H^D is visualized in Fig. 2.9 in a 2D scenario and defined in (2.9). For

Parameter	1D Sequence	2D Sequence	3D Sequence
Drive-Field Amplitude [mT]	12 x 0 x 0	12 x 12 x 0	12 x 12 x 12
Repetition Time [ms]	0.0408	0.6528	21.54
No. Patches	19 x 19	19	-
No. Periods per Patches	1000	1000	-
No. Frames	1	1	1000
Sampling points per Period	102	1632	53856

Table 2.1: *Overview of Scan Sequence Parameters.*

each channel $d \in \{1, 2, 3\}$, equal to spatial dimension sampled, the applied and time-dependent magnetic field strength H^D can be described independently [Kno+18]:

$$H_d^D(t) = A_d \, sin(2\pi f_d t + \frac{\pi}{2}) \, . \tag{2.9}$$

The excitation frequencies are given as the fraction of base frequency, leading to $f_1 = 1250000/102$ Hz, $f_2 = 1250000/96$ Hz and $f_3 = 1250000/99$ Hz. The amplitude is 0.012T or 0T, depending on the number of channels activated and thus on the dimension of the sequence.

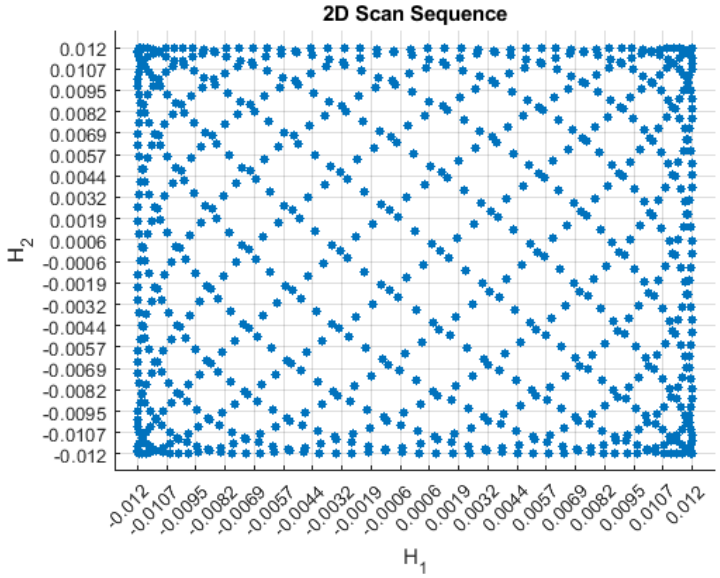

Figure 2.9: *Sampling points of the FFP during one period of the 2D Scan Sequence.* The axis refer to the applied magnetic field strength.

In the further course of this thesis, only 3D data will be used, unless otherwise stated.

2.2.3 *Calibration*

In the measurement-based approach, calibration in order to acquire data for a System Matrix is needed. A special phantom called Delta Sample in the size of an image voxel is the main part of the calibration. In the case of the Open MPI data, it is a cube of size $2mm \times 2mm \times 1mm$ filled with Tracer Perimag in a concentration of 100mmol/l.
Using the Delta Sample as a calibration phantom at specific predefined positions on a 3D grid, the system response is measured at each position. The Delta Sample used in this study was moved and measured at $19 \times 19 \times 19$ grid positions during the calibration process, covering a volume of size $24mm \times 24mm \times 12mm$ [Kno+20]. The Delta Sample is first moved by a robot.After each 19 scanned Delta Sample positions in x-direction, a background scan with the scanner empty is performed to capture background noise. An additional empty scan is performed at the beginning to ensure that there is an empty scan before and after the measurement of a new set of 19 scans in the x-direction. This process is time-consuming, mainly because of the robot movements. For instance, in order to scan the $19 \times 19 \times 19$ grid, $19^3 = 6859$ robot positions have to be scanned. In addition to that, $19 \times 19 + 1 = 362$ background measurements have to be acquired for which the delta sample has to be removed from the scanner.
Each position is scanned with 1000 periods of the Lissajous-type scan trajectory.
In the end, the mean of 1000 voltage time-series of each Delta Sample position and the mean of all background measurements is Fourier transformed. The Fourier coefficients are stored as data in the calibration data set.

2.2.4 *Phantoms*

In addition to calibration measurements of a delta sample to create the system matrix, OpenMPIData provides measurements of three different phantoms, which are presented in this section. For a detailed description, see the original https://media.tuhh.de/ibi/openMPIData/, accessed on April 12, 2023.
In the case of phantom measurements of the 3D sequence, 1000 frames are measured first. Then 1000 frames of the empty scanner are measured to obtain information about the background noise.
The three phantoms Resolution Phantom, Shape Phantom and Dilution Phantom are shown in Fig. 2.10.
The Resolution Phantom consists of 5 tubes, each 1mm in diameter, filled with Perimag tracers of 50mmol/l concentration. Sharing a common origin, the angles of the tubes are chosen differently. One tube is placed along the y-axis, the other tubes have their own angles. Tubes of the XZ-plane have small angles of 10 and 15 degrees, while the other two tubes in the XY-direction have angles of 20 and 30 degrees.
When viewing the XZ-plane, the tubes are imaged at different distances. The

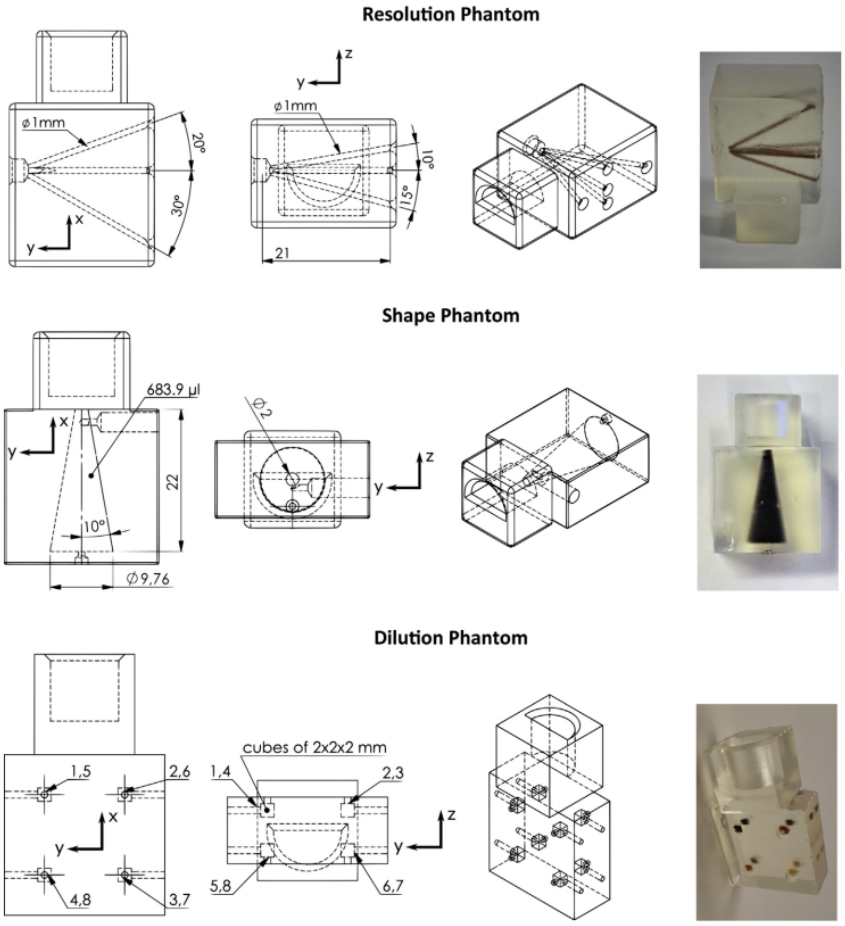

Figure 2.10: *Phantoms used in the open MPI datasets.* Source: [Kno+20]

resolution of the scanner and the image reconstruction method can be determined based on the distinguishability of the tubes.
The shape phantom consists of a cone defined by a radius tip of 1mm and apex angle of 10 degrees. With a height of 22mm, the total volume of the phantom is 683.9μl. It was filled with Perimag tracer in a concentration of 50mmol/l.
Cut in its layers, the cone is viewed as a circle (YZ-plane) or triangle (XY-plane, XZ-plane). Consequently, properties like edge-preserving can be analyzed by evaluating scans of this phantom.
The Dilution or Concentration phantom consists of 8 cubes, each with an edge length of 2mm. The cubes are filled with different dilutions of tracer solution. This allows the sensitivity of the system to be checked. The Concentration phantom was not considered in this thesis.

3

METHODS

3.1 DATA PREPROCESSING

Under ideal conditions, the MPI problem in the measurement-based approach can be expressed as a linear problem, consisting of System Matrix S, Fourier transformed and background corrected received voltage signal u and unknown concentration c (2.8).
In reality, physical factors influence the measured data. This leads to the MPI problem (3.1) with noisy System Matrix A and noisy vector of Fourier coefficients y^δ of the voltage signal:

$$Ac = y^\delta, \quad \text{with } y^\delta := u + b_y + \eta_y \text{ and } A := S + b_A + \eta_A \tag{3.1}$$

Additive systematic background signal b is mainly produced by the time-dependent drive field and perturbances in the measurement chain. Therefore, background signal b_A of the data in the system matrix and time-signal of phantom scans b_y will not be equal but can be estimated by measurements with an empty scanner.
Furthermore, another noise component $\eta \sim \mathcal{N}(\mu, C)$ is added to measured signals. It is assumed to be normally distributed with mean value μ and covariance matrix C, although there is no proof so far that this noise distribution reflects reality.
As a consequence, measured data should be preprocessed in order to achieve reasonable results. In the following sections, several preprocessing steps are described, closely following [KJ19]. In the course of this thesis, the preprocessing steps were implemented in Matlab.
The examples given refer to the Open MPI Data scanned with a 3D-sequence. The calibration data set is *data/calibrations/3.mdf* , phantom data *data/measurements/<phantom>/3.mdf*.

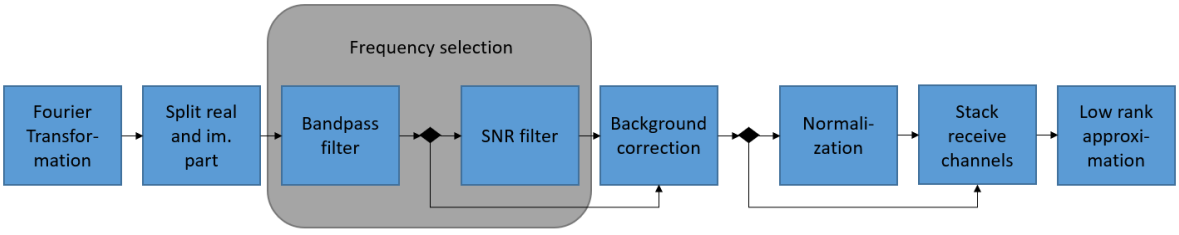

Figure 3.1: *Preprocessing steps applied to MPI data.* The steps follow the preprocessing steps described in [KJ19].

The preprocessing steps applied to MPI scan data are visualized in Fig. 3.1 and described in the following section. All preprocessing steps are always applied to both calibration and phantom scan data. Preprocessing steps SNR filtering and normalization are optional.

Fourier transformation

The calibration data are already Fourier transformed whereas phantom data are stored as time-series. For that reason, the phantom data are Fourier transformed.

Afterwards, a split of real and imaginary part of the complex Fourier coefficients is applied to both calibration and measurement data.

Frequency selection

A frequency selection ensures that frequencies knon to be unsuitable are not used for the reconstruction. Reasons for this can be the known systematic strong noisy frequencies of the measurement chain, or frequencies with generally low signal to noise ratio.

In the case of the OpenMPI data and the scanner used in the generation of the dataset, the absolute mean and variance of the 1000 background measurements of the shape phantom of receive channel 1 are shown in Fig. 3.2. Due to an analog filter, the measurement data show very high variances at frequencies below 75kHz. For that reason, frequencies lower than 80kHz are excluded.

In addition, a frequency selection can be made based on the signal to noise ratio. In contrast to [KJ19], the estimated SNR provided in the data were used. Frequencies with an SNR lower than a certain threshold τ are excluded from the reconstruction.

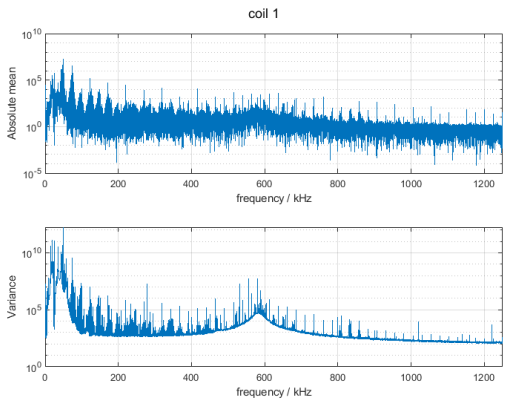

Figure 3.2: *Frequency analysis of receive coil* 1 *of the real part of Fourier transformed background measurements from the Shape phantom scanned with a* 3*D sequence.* The data analyzed are part of the OpenMPIData initiative [Kno+20].

Background correction

A background correction is applied in order to exclude the background signal b. Calibration data and phantom data are treated separately due to the different collection of background measurements.

Before and after the measurement of the delta phantom at each position of a line along x-direction, a measurement without phantom is performed in

the scanner. Applied to the used data, this means after measuring the Delta Phantom at each of the 19 positions along the x-axis.
The calibration process is time-consuming. Especially the robot movements to the precise locations take their time. In the example of the used data, $19^3 = 6859$ different positions have to be scanned. If a finer grid or a larger volume should be calibrated, the number of positions and the calibration time increase accordingly.
The background signal does not only consist of a systematic, static part but it is also assumed to be dynamic. For that reason, background scans using a scanner being empty are not only acquired in the beginning and at the end of the calibration process. Moreover, after a certain amount of calibration scans have been measured, a new set of background scans is performed. In case of the used data, the robot is first moved in x-direction and scans with the delta sample at each of the 19 positions of the grid. After that, the Delta Sample is moved outside the scanner and background scans are performed. Then the Delta Sample is moved inside the scanner, shifted one position in y-direction and calibration scans at each position along x-direction are performed. Afterwards, a new set of background scans with an empty scanner is performed. The many sets of background scans are acquired to allow a background correction of the assumed dynamic background signal. Each Delta Sample scan is background corrected with the two temporal nearest background scans. This is implemented as a convex combination of the previous background scan $b_{previous}$ and following background scan $b_{following}$ for each delta sample scan u_{DS} at position part $i = \frac{1}{19}, \frac{2}{19}, \frac{3}{19}, ..., 1$: $u_{DS;corrected} = u_{DS} - (ib_{previous} + (1-i)b_{following})$.
In the phantom measurements, 1000 frames with phantom in the scanner are measured first, followed by 1000 frames of the empty scanner. For the estimation of b, the 1000 background frames are averaged. Then the average value per Fourier coefficient is subtracted from the averaged scans with phantom:

$$Ax = y^\delta - \mu \, . \tag{3.2}$$

Normalization: "Whitening" estimation of diagonal covariance
To filter out frequency components with particularly high noise content, the noise content $\eta \sim \mathcal{N}(\mu, C)$ is determined by estimating the variance of the 1000 blank measurements of phantom data. The estimation of variance leads to the diagonal covariance matrix C_{diag}. Calculating the reciprocal of the diagonal values of C gives normalization matrix W. Then, both sides of the equation are normalized by multiplying the matrix W, which is called whitening in [KJ19]:

$$WAx = W(y^\delta - \mu), \text{ where } C_{diag} = \begin{pmatrix} \sigma_1^2 & & 0 \\ & \ddots & \\ 0 & & \sigma_M^2 \end{pmatrix}, W = \begin{pmatrix} \frac{1}{\sigma_1^2} & & 0 \\ & \ddots & \\ 0 & & \frac{1}{\sigma_M^2} \end{pmatrix} \tag{3.3}$$

Stack Receive Channels
If data from multiple receive channels are used for reconstruction, they must be stacked to create the system matrix meaning that rows are added to the SM.
Low Rank Approximation of the System Matrix
The system matrix can become quite large. For instance, the system matrix of the $3D$ $19 \times 19 \times 19$ calibration data with applied bandpass filter of frequencies [80kHz 625kHz] lead to a system matrix of size 70446×6859. This can challenge computing capacity and runtime of reconstruction algorithms. To tackle this, a singular value decomposition of the normalized SM WA can be performed:

$$WA = U\Sigma V^T \tag{3.4}$$

To decrease the size of the resulting SM, the first k singular values are used for reconstruction. Applied to the MPI equation of normalized and background corrected system matrix WA and normalized, background corrected scan data $W(y^\delta - \mu)$, the MPI equation is [KJ19]:

$$U_k^T WAx = U_k^T W(y^\delta - \mu) \, . \tag{3.5}$$

Since each column of U_k with index larger than k is cut, the dimension can be reduced strongly. For instance, in [KJ19] $k = 2000$ were used. Setting $k = 2000$, the original system matrix of size 70446×6859 is decreased to 2000×6859.
Singular values of the background-corrected and whitened SM of the 3D calibration data are visualized in Fig. 3.3, where the vertical axis is on a logarithmic scale. This shows a strong decrease of the singular values. This indicates that even a few singular values can be used for reconstruction. In Fig. 3.3, it is shown that the condition number in this example is in the range of $8 \cdot 10^3$. A high condition number indicates an ill-conditioned problem meaning that a small perturbations in the measured date, for instance caused by noise, can lead to comparatively large perturbations in the reconstruction [Dem87].

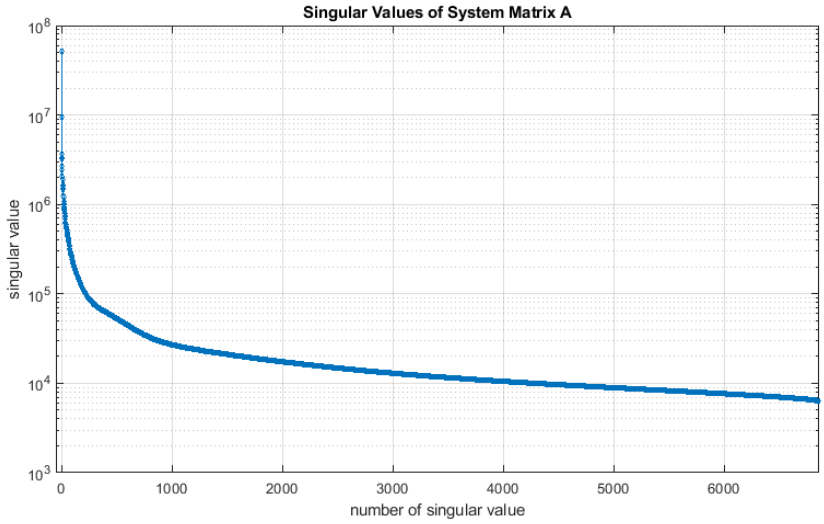

Figure 3.3: *Singular value decay of a normalized and background corrected System Matrix.* Open MPI Datas Calibration Data measured with a 3D sequence are used. Note the logarithmic scale on the vertical axis.

3.2 RECONSTRUCTION AND REGULARIZATION TECHNIQUES

From a Bayesian perspective, regularization problems can be expressed as a Maximum A Posteriori (MAP) problem (3.6) [Zha+], where x is the original solution. In terms of image denoising, this would be a noise-free image, in the MPI problem it is the true concentation distribution of SPIO. The degraded observation $y = \mathcal{T}(x) + \eta$ is in the MPI context the scan data with noise $\eta \sim \mathcal{N}(\mu, \sigma)$ and the measurement-based MPI operator $\mathcal{T}(x) = Ax$ is equal to a multiplication with the System Matrix A. The energy minimization problem is regularized by a regularizer $\mathcal{R}(\cdot)$ and regularization parameter λ:

$$\begin{aligned} MAP: \ \hat{x} &= \underset{x}{argmax}\ p(y|x)\ p(x) \\ &= \underset{x}{argmin} - log\ p(y|x)\ - log\ p(x) \\ &= \underset{x}{argmin}\ E(y;x) + \lambda \mathcal{R}(x) \end{aligned} \tag{3.6}$$

Finally, the problem consists of a y-dependent data term and a regularization term. This regularized energy minimization approach can be used to solve ill-posed problems.

3.2.1 *Ill-posed problems*

According to [TA77], problems are well-posed if the following properties apply to problems in the form of $Ax = y$:

1. a solution x exists;

2. solution x is unique;
3. solution x is stable relative to small changes in the initial data.

If one of these requirements is not fulfilled, it is ill-posed.
In order to solve ill-posed problems and thus compute stable solutions, regularization techniques are necessary.

3.2.2 *Tikhonov regularization*

A widely used method to solve ill-posed inverse problems, more precisely linear equations in the form of $Ax = y$, is the Tikhonov regularization.
Without any regularization, such a problem can be adressed via the Ordinary Least Squares (OLS) approach (3.7), where $\|\cdot\|_2$ is the Euclidean norm:

$$\frac{1}{2}\|Ax - y\|_2^2 \tag{3.7}$$

To add stability of the computed solution, regularization is applied. The corresponding Tikhonov functional with some matrix Γ is:

$$\frac{1}{2}\|Ax - y\|_2^2 + \|\Gamma x\|_2^2 \,. \tag{3.8}$$

Often, the matrix is defined as $\Gamma = \alpha I$, a scalar multiple of the identity matrix with regularization parameter α (cf. [CR04]):

$$\frac{1}{2}\|Ax - y\|_2^2 + \frac{\alpha}{2}\|x\|_2^2 \,. \tag{3.9}$$

The L^2-norm of x is added as penalty term [Ger21], leading to a ridge regression. It is also possible to instead add the L^1-norm of x as penalty term, leading to a Least Absolute Shrinkage and Selection Operator (LASSO) regression.
In order to solve (3.9), the term is minimized with respect to x (cf. [CR04]):

$$\hat{x} = \min_x \left\{ \frac{1}{2}\|Ax - y\|_2^2 + \frac{\alpha}{2}\|x\|_2^2 \right\} \,. \tag{3.10}$$

The optimality condition is

$$A^*(A\hat{x} - y) + \alpha\hat{x} = 0 \,, \tag{3.11}$$

leading to the solution

$$\hat{x} = (A^*A + \alpha I)^{-1}A^*y \,, \tag{3.12}$$

where A^* is the adjoint of A.
To get the best result $\hat{x}$, the regularization parameter α should be optimized. Applied to the MPI problem, the best regularization parameter α is identified by comparing the resulting concentration vector $\hat{x}$ with a ground truth

and then minimizing the error or maximizing an image quality measure like PSNR or SSIM, which are introduced in Chapter 3.3. A ground truth is the true concentration distribution of the scanned object. In the example of the used data, the phantom, phantom position and concentration of Tracer solution is known so that a ground truth can be calculated.
This regularization applied to MPI data is implemented in Python.

3.2.3 *Learning-based techniques*

In addition to standard approaches, there are Machine Learning-based techniques to find a regularized solution to the problem $Ax = y$. In the following section, two Learning-based regularization techniques, Deep Image Prior (DIP) and Plug and Play Prior (PnP) with a deep Convolutional Neural Network (CNN) as a denoiser are described. Learning-based techniques can overcome some drawbacks of traditional techniques like reduced contrast when applied to MPI [Sha+22].

3.2.3.1 *Deep Image Prior (DIP)*

First introduced in 2017 [UVL20], DIP found some popularity because, unlike traditional Deep Learning methods, it does not require a large amount of data. In fact, only one image or one set of measured data is necessary. In the original paper of Ulyanov [UVL20], DIP is used to tackle standard inverse problems like denoising, inpainting and super-resolution. In other publications, DIP has been used for reconstruction in clinical settings such as CT [BLS20], MRI [Yoo+], and MPI [Dit+].

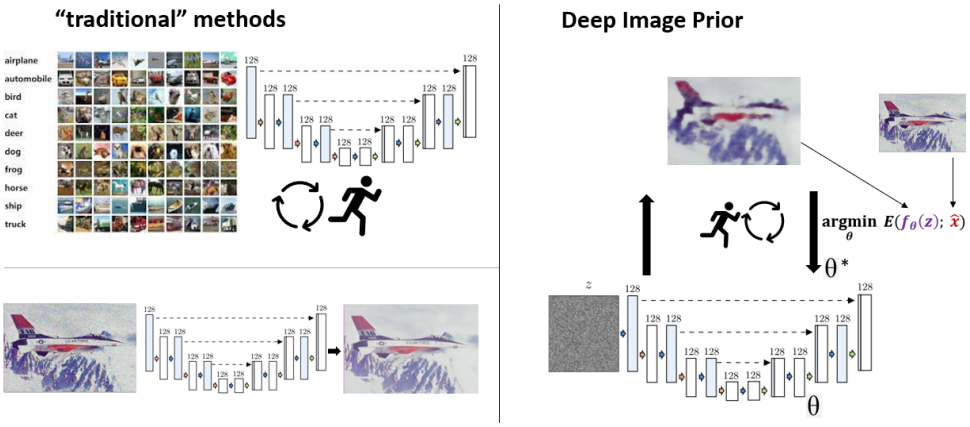

Figure 3.4: *Comparison of "traditional" deep learning techniques vs. the Deep Image Prior method.* "Traditional" supervised deep learning techniques use a huge amount of labelled data or corrupted-uncorrupted data pairs [Kri12]. These are the basis to iteratively set the weights of a network [BLS20]. Feeding an unknown corrupted image [GMHAHE20] forward the already trained net, an uncorrupted image is expected as output. The Deep Image Prior method iteratively sets weights of an untrained net using a noisy input with the goal to decorrupt an image using a task-dependent prior.

In Fig. 3.4, the difference between "traditional" deep learning techniques in order to denoise an image and the Deep Image Prior method is shown. Usually, a large set of corrupted and ground truth data are needed to train a network. For this, several training iterations are run. After training, the network parameters are fixed. Then, an unknown, corrupted image is passed through the network and a denoised version is received.
The idea of DIP is rooted in energy minimization problems (3.6), consisting of a task-dependent data term and a regularizer.
Input of DIP is a noisy image or a noisy vector z. The special feature of z is that it is initialized with random values, in the MPI DIP implementation sampled from a uniform distribution $z \sim U[0\ 0.7)$.
Equation (3.13) shows that DIP also minimizes the energy. However, what is special here is that concentration vector $x = \varphi_\theta(z)$ is expressed as the result of the image z processed by a CNN $\varphi_\theta(z)$ with parameters θ. The ultimate goal of DIP is to find a set of parameters θ that transforms the noisy input z to an output, so that the applied task-dependent prior is very close to y^θ. To fit the task-dependent term to the MPI problem, $\varphi_\theta(z)$ is multiplied by the system matrix A, which results in the minimization problem:

$$\min_\theta \|A\varphi_\theta(z) - y^\delta\|_2^2 \ . \tag{3.13}$$

This means, that the feedthrough of a CNN given a noisy input z is a discrete concentration distribution c. $A\varphi_\theta$=Ac=y is in MPI the expected measured voltage data y. To ensure that the calculated concentration distribution is the one that fits the actual scan data y^δ, the L^2-norm is minimized. Since random but noisy input z and the architecture of CNN φ is set at the beginning and in the learning process not changed, there are only the weights θ that can be adjusted in the learning process and thus have an influence on the calculated concentration distribution.
Since an explicit computation of the best parameters θ would be too computationally intensive, they are first randomly initialized and then iteratively fitted via a method like gradient descent [UVL20]. Therefore, hyperparameter step size can be adjusted.
In case of DIP, the CNN works implicitly as a prior: It has been shown that the quality of the result is strongly influenced by the chosen network architecture [UVL20] since the architecture determines the solution space and how it is searched. Moreover, low frequent parts like large lighter and darker areas of an image are reconstructed first. After more iterations, higher frequent parts like edges, smaller details and noise of an image are shown in the DIP output which finally lead to overfitting. In some cases, early stopping of DIP leads to a denoised result [UVL20]. As a consequence, the regularizer does not need to be defined explicitly.
Based on the DIP implementation for MPI in Python from the authors of [Dit+], the DIP results analyzed in the further course of this thesis were computed.

3.2.3.2 *Plug and Play (PnP)*

Plug and Play Priors is a framework that has been first introduced in [VBW13] and stands out for its flexibility and customizability for denoising problems. It consists of two parts that are usually computed in many iterations: Reconstruction and denoising. Applied to MPI, first a concentration distrubution is calculated by finding a solution to the system of linear equations. Afterwards, the result is denoised. Both reconstruction and denoising are performed during each iteration of the PnP. In order to allow a gradual improvement of the results, the denoiser takes the previous reconstruction into account and the reconstruction of one iteration is influenced by the denoised result of the previous iteration.
Different algorithms can be plugged in to reconstruct or denoise. For instance, a denoiser can be implemented by a standard approach like soft thresholding or exchanged with a more complex denoiser like a denoiser CNN.
The Plug and Play approach iterates between reconstruction and denoising. The latter regularizes the solution of the reconstruction part. In the next iteration, the result of the denoiser influences the reconstruction.
In the following section the functionals of the reconstruction and the denoiser are described. The functionals are based on the energy minimization problem of the measurement-based approach to MPI. Afterwards, the implemented hyperparameters are introduced.
Applied to the MPI problem, the estimation of the discrete SPIO concentration distribution $\hat{x}$ can be expressed as the minimization problem

$$\hat{x} = \underset{x}{arg\,min} \frac{1}{2\sigma^2}||y - Ax||^2 + \lambda\mathcal{R}(x) \ , \tag{3.14}$$

which is a reformulation of (3.6) [Zha+] with System Matrix A, background-corrected scan data $y = Ax + \eta$, normal distributed noise $\eta \sim \mathcal{N}(\mu, \sigma)$ and a Regularizer $\mathcal{R}(x)$ with positive regularization parameter λ.
The data term and regularizer can be decoupled by introducing an auxiliary variable z, which should equal x. This leads to

$$\hat{x} = \underset{x}{arg\,min} \frac{1}{2\sigma^2}||y - Ax||^2 + \lambda\mathcal{R}(z) \quad s.t. \ \ z = x \ \ . \tag{3.15}$$

This problem can be solved by minimizing the Lagrangian and introducing penalty parameter μ according to [Zha+]:

$$\mathcal{L}_\mu(x, z) = \frac{1}{2\sigma^2}||y - Ax||^2 + \lambda\mathcal{R}(z) + \frac{\mu}{2}||z - x||^2 \ \ . \tag{3.16}$$

This is implemented by splitting the term according to the Half Quadratic Splitting method (HQS) method:

$$x_k = \underset{x}{arg\,min}||y - Ax||^2 + \mu_k\sigma^2||x - z_{k-1}||^2 \tag{3.17}$$

$$z_k = \underset{z}{arg\,min}\frac{1}{2(\sqrt{\frac{\lambda}{\mu_k}})^2}||z - x_k||^2 + \mathcal{R}(z) \quad . \tag{3.18}$$

First, the reconstruction problem is solved (3.17), then the solution is denoised (3.18) [Zha+] at each iteration k. The algorithm iterates between these two steps.
Each step of the splitting is a minimization problem that can be solved computing the gradient. This can be solved with known methods like Conjugate Gradient (CG) or Alternating Direction Method of Multipliers (ADMM). In this thesis, CG algorithm is implemented.
Subproblem (3.18) works as a denoiser of x_k, with an assumed noise level of $\frac{\lambda}{\mu_k}$ and can thus be expressed as:

$$z_k = Denoiser\left(x_k, \sqrt{\frac{\lambda}{\mu_k}}\right) \tag{3.19}$$

In the spirit of Plug and Play, any denoiser could be plugged in to solve (3.18). In the scope of this work, a shrinking method and a Learning-based method using a deep CNN are implemented in Python. Regarding the CNN, part of the code is based on the work of PhD candidate Tim Selig.
In the reconstruction part of PnP, product $\mu_k\sigma^2$ controls the influence of the regularization condition. For that reason it is implemented as one parameter:

$$\alpha_k = \mu_k\sigma^2 \quad . \tag{3.20}$$

In order to achieve a denoised result, [Zha+] proposes to increase α_k at each iteration k. For MPI, this is implemented by hyperparameter α_{incr} controlling the increment of α for each iteration k,

$$\alpha_k = \alpha + k \cdot \alpha_{incr} \quad . \tag{3.21}$$

Since μ is part of both regularization and denoiser part, the noise level is influenced by α and therefore implemented as

$$\frac{\lambda}{\mu_k} = \frac{\lambda\sigma^2}{\alpha_k} \quad . \tag{3.22}$$

Hyperparameters tuned and implemented in this work are α_{start}, α_{incr} and $\lambda\sigma^2$ and the resulting image quality analyzed over the course of iterations.
Denoising by Shrinking
One simple denoising method is shrinking the values of x_k by applying

function $d(x_k, \beta)$ (3.23). Each element of x_k that is smaller than a certain threshold β is set to 0. Otherwise, the value is decreased by β.

$$z_k = d(x_k, \beta) \; with \;\; d(x_k(i), \beta) \begin{cases} 0, & \text{if } x_k(i) < \beta \\ x_k(i) - \beta, & \text{otherwise} \end{cases} \tag{3.23}$$

Assuming that the noise level is lower than the signal, this function is a denoiser.

Denoising using a Convolutional Neural Network

In 2020, [Zha+] introduced a deep CNN called DRUNet denoiser prior that

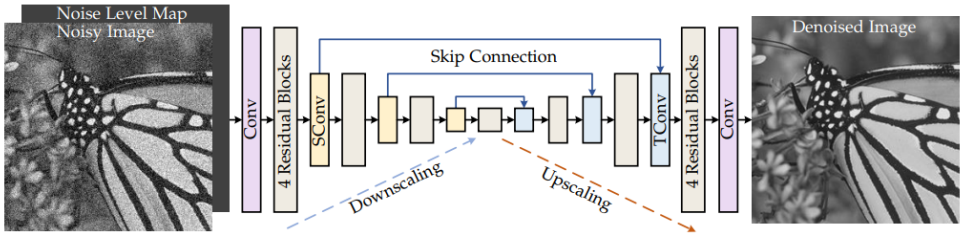

Figure 3.5: Architecture of the deep CNN DRUnet denoiser prior. In addition to an input image, the net takes a Noise Level Map in order to receive a Denoised Image. Strided convolution "Sconv" and transposed convolution "Tconv" blocks are used. [Zha+]

successfully performed in image restoration tasks such as denoising. The pretrained parameters are freely accessible on https://github.com/cszn/DPIR/tree/master/model_zoo. An overview over the architecture is given in Fig. 3.5. It is a combination of U-Net [RFB] and ResNet [He+16].

In the scope of this work, this network as well as pretrained parameters are used. Since there are not enough freely accessible MPI data, no transfer learning is applied. Instead, it is tested how well the pretrained CNN works depending on different constant noise levels, regularization and penalty parameters.

Since the input is downsampled four times, the width and height of the input has to be divisible by 2^4. Due to the calibration process and data used, the reconstructed volume of size $19 \times 19 \times 19$ is split into 19 images of size 19×19. In order to fit the necessary size, the input images are padded with edge-padding to result in a size of 32×32. The original 19×19 pixel grid of the output images are then extracted and form the further processed output of the net.

Denoising of a Volume

The denoising network has been designed for 2D images, not for a 3D volume. There is a spatial dependence of the concentration distribution in all 3 directions. Therefore, it is necessary to slice the volume cleverly into images and stitch the results back together into a volume.

If 19 images of each dimension are denoised and then the volume is regenerated via averaging, the valuable edge preservation is probably lost. Therefore, this method is not used.
If one always slices along the same dimension, artifacts are to be expected, which are probably reflected in different basic brightness of the individual layers.
There is another option to denoise a volume which mainly consists of choosing a random axis to slice the volume at each iteration. The process is visualized in Fig. 3.6. The reconstructed volume is sliced into separate images along a randomly chosen axis. Then, the resulting images are denoised independently. Having been denoised, the images are stiched back in the original order to regain a volume. In the case of the used calibration data, 19 images

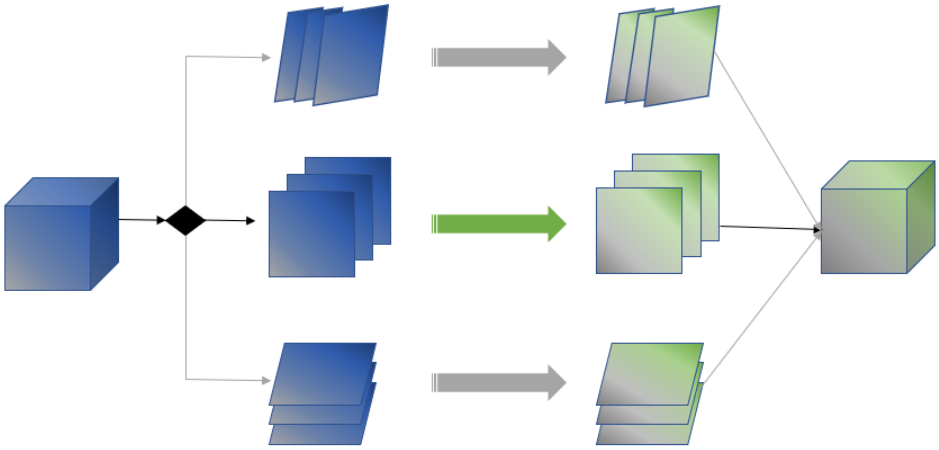

Figure 3.6: *Denoising along a randomly chosen axis.* A reconstructed volume (blue cube) is sliced along a randomly chosen axis (black arrow). The resulting images (blue squares) are denoised independently (green arrow). The denoised images (green squares) are then stitched back to a volume (green cube).

are received that are denoised independently.
Since a new random number and thus a random axis to slice is chosen at each iteration, artifacts caused by slicing are expected to be reduced.

3.3 IMAGE QUALITY MEASURES

This section explains standard image quality metrics that will be used to evaluate and compare the results later in this thesis. These include the Peak Signal to Noise Ratio (PSNR) and Structural Similarity (SSIM) metrics.

3.3.1 *Peak Signal to Noise Ratio (PSNR)*

The Mean Squared Error (MSE) of two images $f \in \mathbb{R}^{MxN}$ and $g \in \mathbb{R}^{MxN}$ with $M, N \in \mathbb{N}$ is calculated via the mean of the squared difference of each image pixel [HZ10]:

$$MSE(f,g) = \frac{1}{MN} \sum_{j=1}^{M} \sum_{i=1}^{N} (f_{ij} - g_{ij})^2 \, . \tag{3.24}$$

For the 3D case, the MSE of two volumes $f \in \mathbb{R}^{LxMxN}$ and $g \in \mathbb{R}^{LxMxN}$ with $L, M, N \in \mathbb{N}$ is calculated via the mean of the squared difference of each volume voxel:

$$MSE(f,g) = \frac{1}{LMN} \sum_{k=1}^{L} \sum_{j=1}^{M} \sum_{i=1}^{N} (f_{ijk} - g_{ijk})^2 \, . \tag{3.25}$$

Taking into account the MSE and maximum fluctuation R of the reference image or volume g, the Peak Signal to Noise Ratio (PSNR [HZ10]) is a image quality measure of logarithmic scale:

$$PSNR(f,g) = 10 \, log_{10}(R^2/MSE(f,g))[dB] \quad . \tag{3.26}$$

The higher the PSNR, the better the signal to noise ratio.
There are different approaches to set R. In this implementation, R is the difference of the highest and lowest voxel value of reference image or volume g.
Applied to the results of the different regularization methods, volumes are compared. In this case, the reference volume is the true and known concentration distribution of the scanned phantom. Since there might be deviations from the expected position of the phantom and thus ground truth x_{ref}, position uncertainty is taken into consideration [KJ20]:

$$PSNR_{max}(x) = \max_{\Delta r \in \mathcal{R}} PSNR(x, x_{ref,\Delta r}) \, , \tag{3.27}$$

where position shifts Δr with a step size 0.5mm in the neighborhood of $[-3mm \; 3mm]^3$ each lead to a reference volume $x_{ref,\Delta r} \in \mathcal{R}$, in total 2197 reference volumes. PSNR of the reconstructed volume x and reference volume $x_{ref,\Delta r}$ is calculated. The largest one is defined as $PSNR_{max}$.

3.3.2 *Structural Similarity Index Measure (SSIM)*

The Structural Similarity Index Measure (SSIM) describes the preserved structural information of a reconstructed volume compared to a ground truth. Three factors are considered: Luminance (l), contrast (c) and structure (s) [HZ10]:

$$\begin{aligned} l(f,g) &= \frac{2\mu_f\mu_g + C_1}{\mu_x^2 + \mu_y^2 + C_1}, \\ c(f,g) &= \frac{2\sigma_f\sigma_g + C_2}{\sigma_x^2 + \sigma_y^2 + C_2}, \\ s(f,g) &= \frac{\sigma_{fg} + C_3}{\sigma_f\sigma_g + C_3} \quad , \end{aligned} \tag{3.28}$$

where μ_f is the mean value, σ_f standard deviation of f and covariance σ_{fg} of f and g.
The three factors l, c and s can be weighted in order to calculate SSIM:

$$SSIM(f,g) = [l(f,g)]^\alpha \cdot [c(f,g)]^\beta \cdot [s(f,g)]^\gamma \tag{3.29}$$

Weights α, β, γ are all set to 1. Constants C_i, $i \in 1,2,3$ avoid division by zero and are set to $C_1 = (0.01 \cdot R)^2$, $C_2 = (0.03 \cdot R)^2$ and $C_3 = 0.5 \cdot C_2$ with dynamic range R. As in the implementation of [Dit+], R is set to 100 representing the concentration of the Delta Sample being used during the calibration process.
The value range of SSIM extends from -1 (no similarity) to 1 (perfect match). Analogous to equation (3.27), the compared ground truth contains uncertainty, which leads to uncertainty-aware measure $SSIM_{max}(x)$ [KJ20]:

$$SSIM_{max}(x) = \max_{\Delta r \in R} SSIM(x, x_{ref,\Delta r}) \; . \tag{3.30}$$

Precalculated reference values kindly provided by T. Kluth were used, which were the ground truth in the calculation of the image quality measures in [Dit+].

4

RESULTS

In this chapter, the results of the regularization methods L^2-regularization, DIP and PnP of different hyperparameters are presented. Using the image quality parameters SSIM and PSNR they are evaluated and compared. Different preprocessed data are used as described in the previous chapters. First, reference values which represent part of the ground truth of the different phantoms are shown to provide a basis for comparison. Then, results of the regularization methods are presented and the influence of different hyperparameters on the resulting image quality is investigated.

4.1 REFERENCES

To test different regularization techniques, measurement data from OpenMPIData [Kno+20] was used. For this purpose, measurement data of two phantoms are examined cf. Fig. 4.1: First, that of the Shape phantom, a cone filled with tracers of an SPIO concentration of 50mmol/l. In addition, the Resolution Phantom was used, whose design of tubes filled with tracer solution is well suited for determining the resolution.

In order to create the System Matrix, data from a calibration procedure

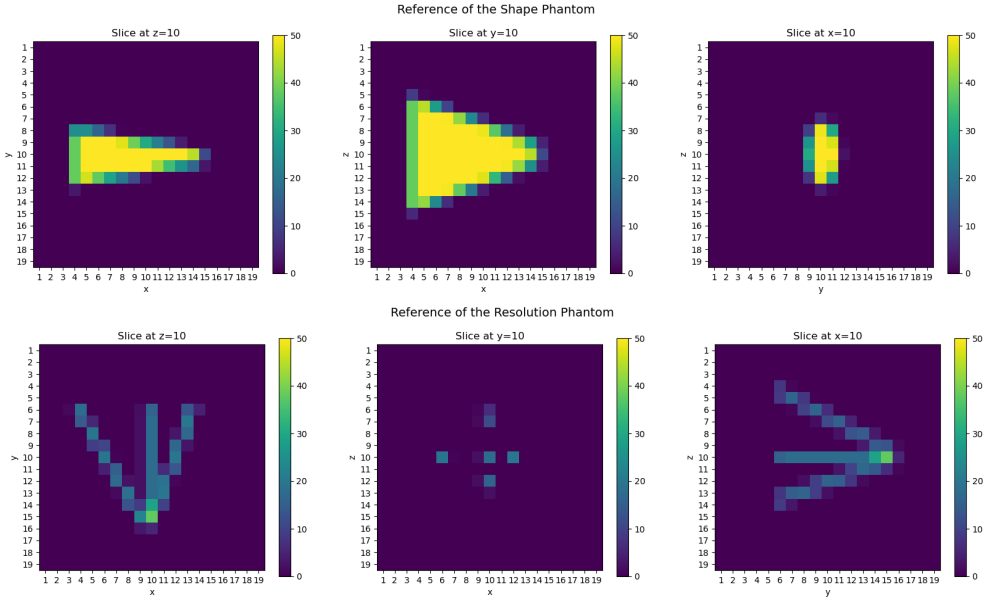

Figure 4.1: *References of the two phantoms used, sliced in each axis.* Top: Shape phantom reference, bottom: Resolution phantom reference. Shape and Resolution phantom data are from the Open MPI data [Kno+20].

is used, which consists of a volume grid of size $19 \times 19 \times 19$ voxels. Thus, the spatial concentration distribution to be reconstructed is calculated in a $19 \times 19 \times 19$ grid.
The middle slices of each axis are shown in Fig. 4.1. Shape phantom is shown in the top row, Resolution phantom in the bottom row. The maximum of the brightness scale is set to the concentration used for the phantom scan of 50mmol/l. The different length of the shape phantom cone in z-direction compared to the other two axis is caused by the smaller size of the Delta Sample used for the calibration scans. Due to its size $2mm \times 2mm \times 1mm$, the voxels are not cubes with the same length. As a consequence, the z dimension appears to be larger in the reconstructed image.
In order to compare reference and reconstructed data, the different value ranges have to be taken into account. Caused by solving a system of linear equations using the SM, the value of the reconstructed concentration vector is relative to the concentration of the calibration phantom Delta Sample. A concentration of 100mmol/l was used as reference phantom for the calibration scans. This means that a value of 0 in the reconstructed data equals a concentration of 0mmol/l, a value of 1 in the reconstructed data corresponds to a concentration of 100mmol/l. As a consequence, the ideal value in the center of a reconstructed shape phantom is 0.5 which corresponds to a tracer concentration of 50mmol/l.
This is also taken into account in the calculation of image quality measures PSNR and SSIM and their respective uncertainty-aware version PSNR_{max} and SSIM_{max}. Prior to the calculation of the image quality measures, the reconstructed concentration distribution is multiplied with factor 100, which is the concentration of the Delta Sample.
In the following sections, reconstruced slices are shown in a relative scale from 0 to 0.75.

4.2 TIKHONOV REGULARIZATION

In this section the results of the implemented Tikhonov Regularization is evaluated based on the described references.
The only value that can be adjusted in the implemented Tikhonov Regularization is regularization parameter α. This means that α is the only parameter that controls the regularization strength and in consequence influences the quality of the reconstruction. The influence of α is analyzed.
Figure 4.2 shows the PSNR_{max} (blue) and the SSIM_{max} (orange) dependent on regularization parameter α. The reconstructed data of this example are neither normalized nor SNR filtered during the preprocessing.
Results of both Shape phantom and Resolution phantom show that a too large α leads to decreased PSNR and SSIM.
In the case of the Shape phantom, the peak values for both image quality measures are caused by similar regularization parameters: The best α of SSIM_{max} is 10^{-4}, the best α of PSNR_{max} is $5 \cdot 10^{-5}$. The difference between the best α can be explained by the evaluated values of α. Due to the discretiza-

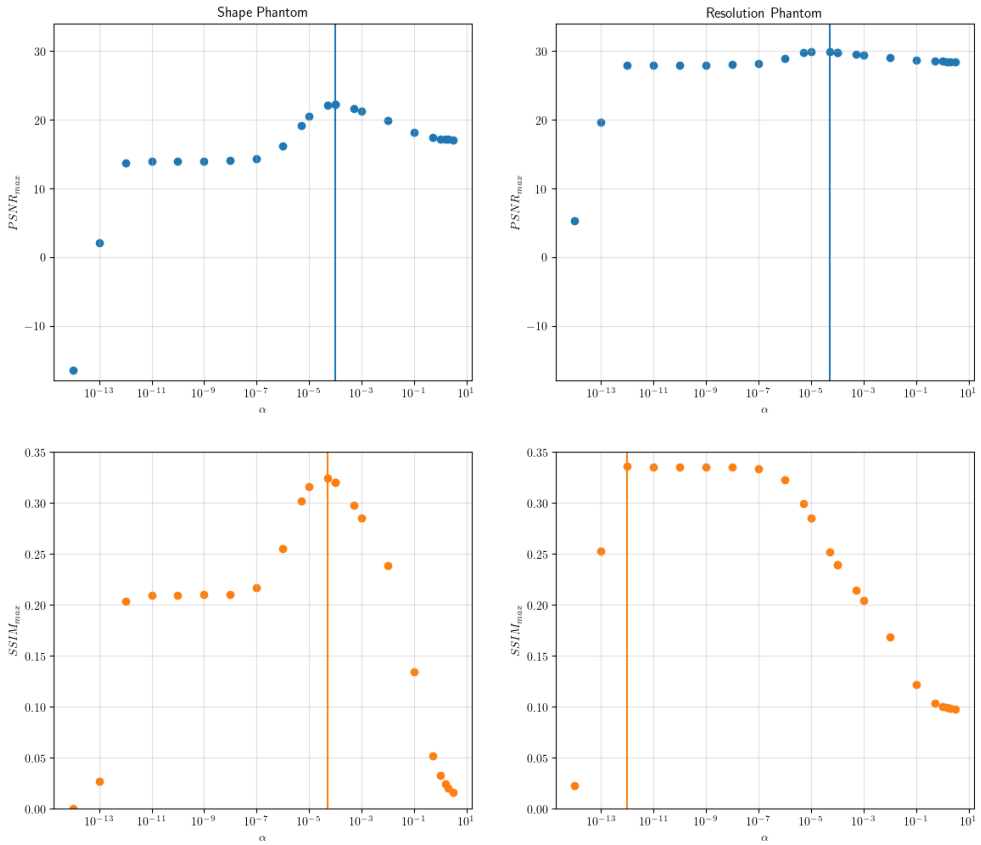

Figure 4.2: *Image quality measures of Tikhonov Regularization Results with different penalty parameter α.* Results of the Shape phantom are shown in the left column, results of the Resolution phantom in the right column. Preprocessing: Non-normalized data without SNR filtering, first 2000 singular values used. The position of the maximum value of $SSIM_{max}$ (orange) and $PSNR_{max}$ (blue) is highlighted by vertical lines. Note the logarithmic scale on the axis representing α.

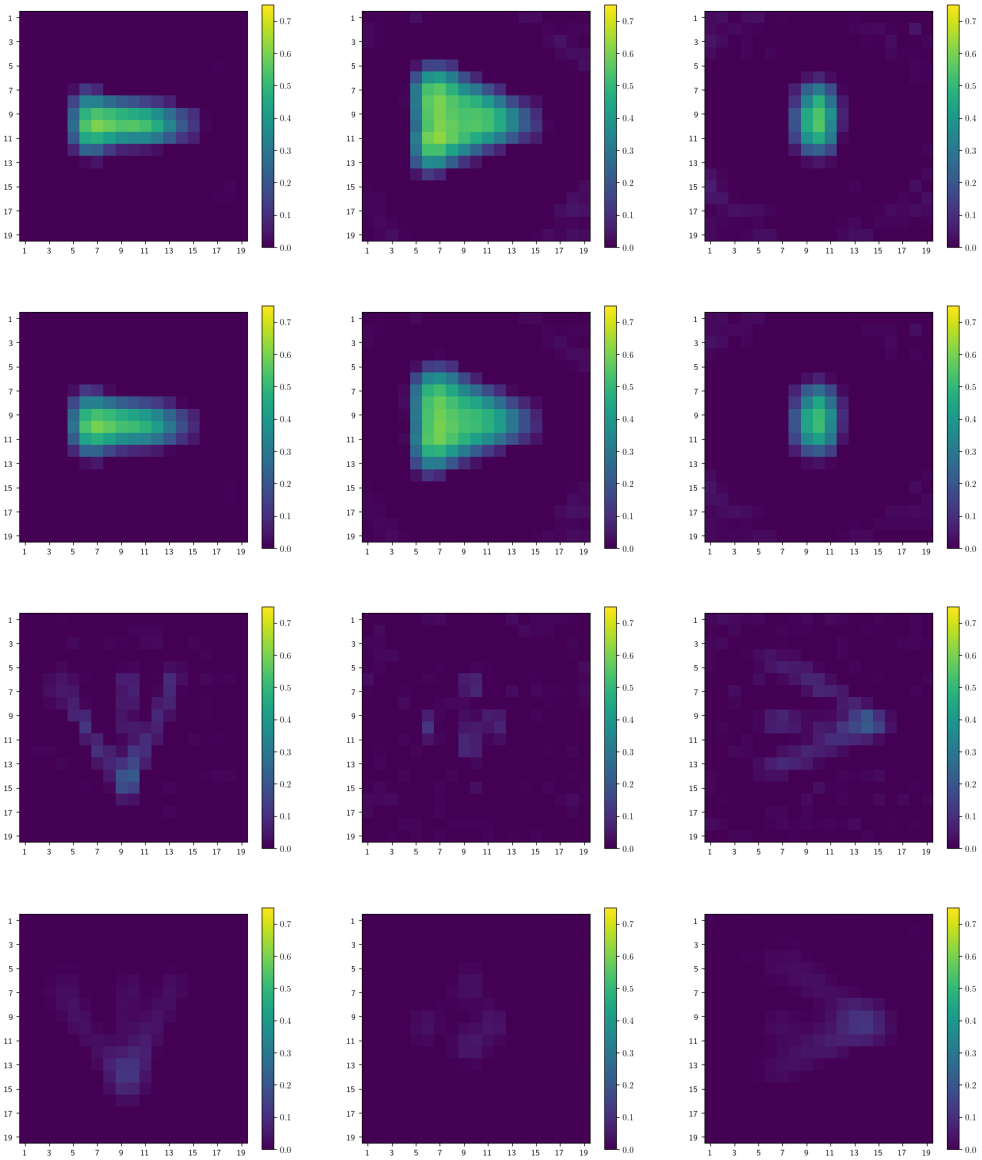

Figure 4.3: *Best results of the L^2 regularization according to* PSNR_{max} *(1^{st}, 3^{rd} row) and* SSIM_{max} *(2^{nd}, 4^{th} row) values.* Regularization parameter α from top to bottom: $5 \cdot 10^{-5}$, 10^{-4}, $5 \cdot 10^{-5}$, 10^{-12}

tion, the overall course of image quality measures is sampled at the analyzed α. The best overall reconstruction might be achieved using a regularization parameter between $5 \cdot 10^{-5}$ and 10^{-4}.

Best regularization parameters leading to the maximization of PSNR_{max} and SSIM_{max} do not necessarily align. An example for that is shown in the evaluation of the Resolution phantom results. According to PSNR_{max}, best α is $5 \cdot 10^{-5}$, whereas SSIM_{max} decreases in this area. SSIM_{max} values are best with the choice of $\alpha \in [10^{-12},\ 10^{-8}]$. Middle slices of the results of the implemented Tikhonov Regularization with best PSNR_{max} (first and third row) and best SSIM_{max} (second and fourth row) are shown in Fig. 4.3. The structures of the Shape phantom are visible although blurred compared to the

reference image. The background is free of noise.
The influence of large regularization parameter $\alpha = 0.01$ is shown in Fig. 4.4

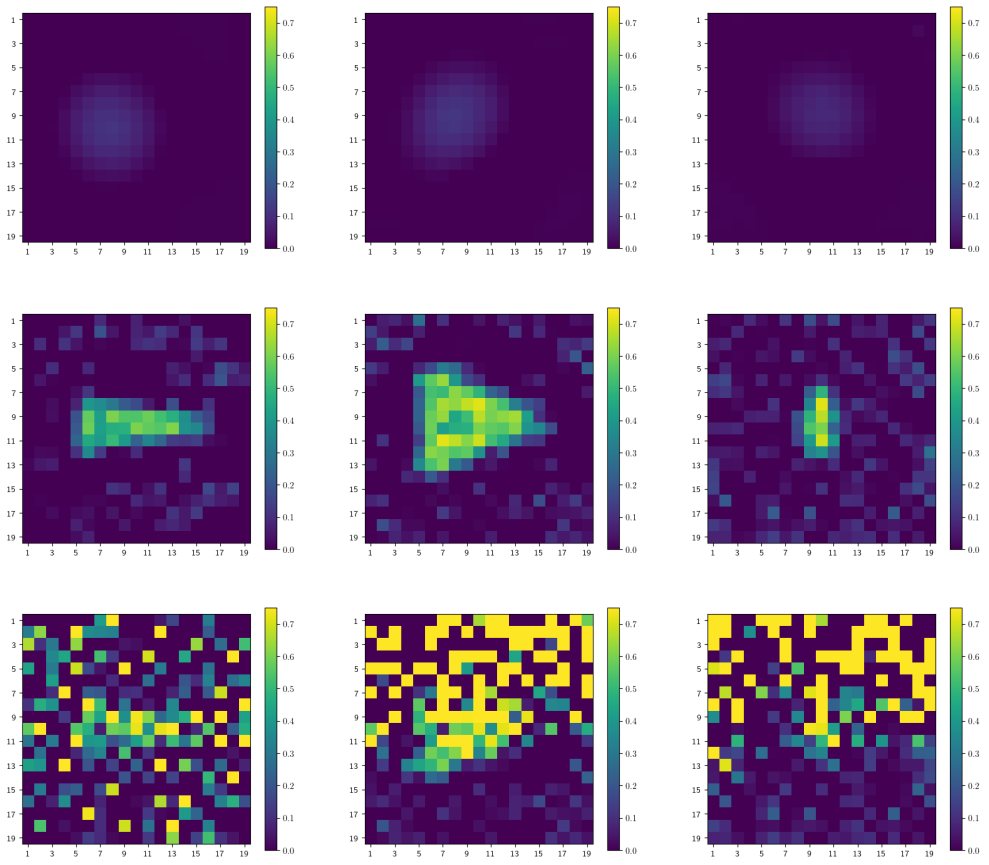

Figure 4.4: *Reconstruction of the Shape phantom with Tikhonov L^2-regularization using not suitable penalty strength.* Regularization parameter α from top to bottom: $0.01, 10^{-10}, 10^{-14}$. The top images show a too weak regularization, whereas on the middle and bottom images the effect of a too strong regularization is shown.

(top). The triangular shape of the phantom is hardly recognizable. Overall, the result has a blurry visual impression and lacks of high frequent image parts. Due to the strong regularization, high frequent parts are suppressed and low frequent parts of the image remain.
On the other hand, if α is chosen too small, high frequent parts are enhanced: Edges are sharper while noise can be seen. This is shown in Fig. 4.4 in the middle row using regularization parameter 10^{-10}. If α is chosen even smaller, noise is strongly enhanced and eventually overcomes signal intensity leading to strong artifacts in the reconstruction. The result of $\alpha = 10^{-14}$ is shown in Fig. 4.4 (bottom).
Having provided a baseline using Tikhonov Regularization, the results of the two Machine Learning-based methods are described in the following subsections.

4.3 DEEP IMAGE PRIOR (DIP)

The Deep Image Prior method is one of the two Machine Learning-based Regularization techniques applied to real scan data from the OpenMPIData [Kno+20]. The first paper where the application of DIP to these data is described was published in 2020 [Dit+]. After contacting the authors, both code and used data were kindly provided.

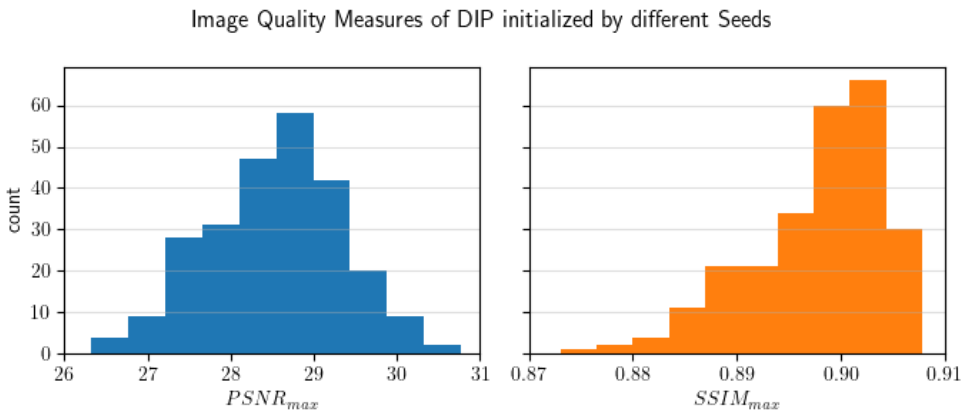

Figure 4.5: *Image quality measures* PSNR_{max} *and* SSIM_{max} *of the DIP result using different seeds.* In total, 250 different seeds are applied. Normalized data of the Shape phantom with SNR-thresholding $\tau = 5$, step size 0.001 and 350 iterations are used for the DIP approach. The image quality measures vary by using different seeds. According to paper: PSNR_{max} 29.94dB, SSIM_{max} 0.973

The image quality measures PSNR_{max} and SSIM_{max} values published in the paper of DIP could not exactly be reproduced although the same preprocessed data and hyperparameters were used. The calculated values of PSNR_{max} and SSIM_{max} do not align. This can have multiple reasons: First, parameters set for the calculation of PSNR and SSIM might differ. The respective parameters in PSNR is the maximal fluctuation R, in SSIM the constants C_1, C_2 and C_3 that might be set differently. Second, the seed in order to set random values can differ. The random state influences both the initial values set of the 3D-net used in Deep Image Prior and the initial values of the randomly set input z. The initial values define the starting point of in the solution space and thus influence which solutions are calculated via gradient descent during the learning process of DIP.
To verify this hypothesis, one subset of preprocessed data is selected and processed with DIP using different seeds. For this experiment, Shape phantom data which is normalized ("whitened") and SNR thresholded with $\tau = 5$. According to [Dit+], an SSIM_{max} of 0.973 and PSNR_{max} of 29.94dB is achieved after 350 iterations and step size 0.001.

In the experiment, 250 different seeds were set. For each seed set, PSNR and SSIM of the result is calculated after 350 iterations with step size 0.001. The result in shown in Fig. 4.5. The published PSNR_{max} value 29.94dB is in

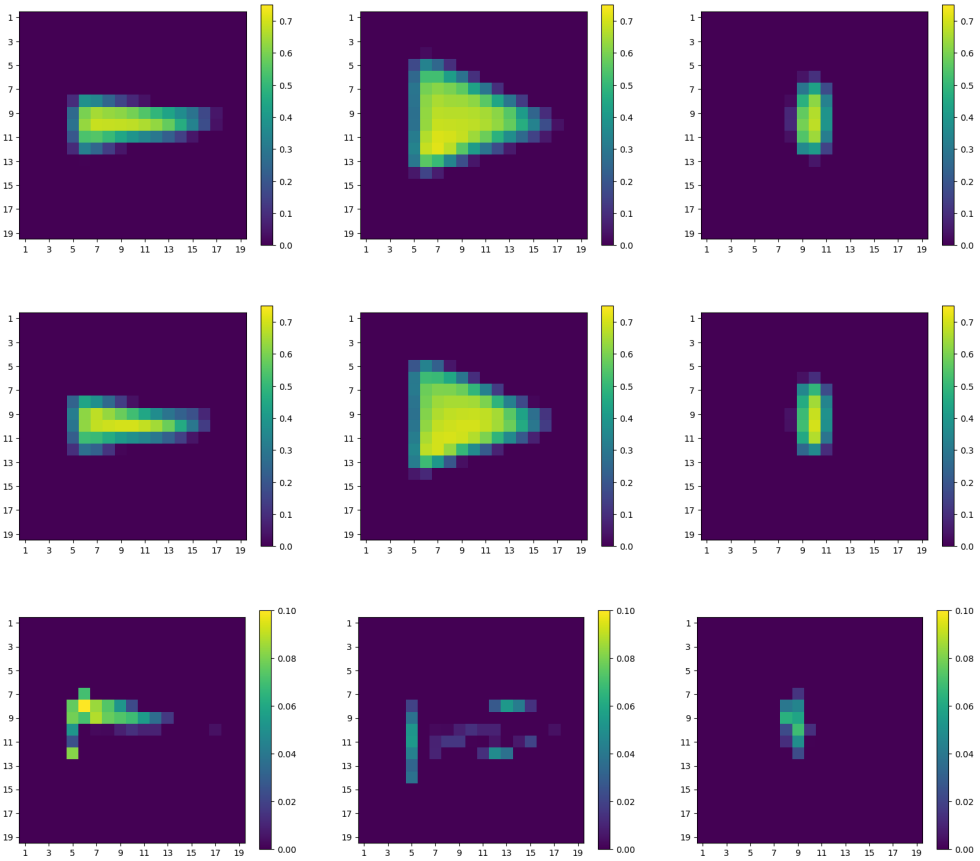

Figure 4.6: *Comparison of the reconstruction of the Shape phantom using the DIP method and different seeds.* Results of DIP SNR threshold 5, normalized Shape phantom. Top: worst PSNR_{max} 26.32dB and SSIM_{max} 0.87 result, middle: best PSNR_{max} result 30.76dB with SSIM_{max} 0.90, bottom: difference of best and worst. Note the scaling of the colorbar.

the range [26.32 30.76]dB of the calculated PSNR_{max} of different seeds. The distribution shows that the published value is in the higher end of the distribution. Followingly, the difference of locally calculated PSNR_{max} results can be explained by the usage of different seeds. Whereas the puplished SSIM_{max} 0.973 of the data is outside the range [0.87 0.90] and many standard deviations apart from the center of the distribution. This indicates, that the difference between published and locally calculated values has rather a systematic cause than the initialization of random values. We conjecture that the parameters C_1, C_2 and C_3 are probably set differently for the computation of SSIM. It was not tried to estimate the used values of C_1, C_2 and C_3, since the results are also influenced by the unknown used seed.
Although the image quality measures differ having set different seeds, the results are visually similar in the case of the analyzed dataset. This is shown in Figure 4.6, where the middle slices of the results with best PSNR_{max} 30.76dB with corresponding SSIM_{max} of 0.87 (top row) and worst PSNR_{max} of 26.32dB with corresponding SSIM_{max} 0.90 are visualized. Since the visible impression is similar, the difference of the reconstructions is shown as well (bottom row).

Note that the scale of the difference is not the same as the one of the original values of the reconstructed slices, since it is vastly smaller than the peak values of the reconstructed concentration.
In summary, computated image quality measures differ from the published values. In order to provide a common ground for comparison, the locally computed values are used and compared to the results of the Tikhonov regularization and Plug and Play results.
The goal of the Deep Image Prior method is to adjust parameters of a CNN so that a randomly initialized input image is passed forward to a desired output (Ch. 3.2.3.1). In case of MPI, this means that a concentraton distribution should be the CNN's output so that multiplied with the system matrix, the result equals scanned phantom data. In this subsection, the influence of different settings during the training process is analyzed. This includes image quality measures after a different number of training iterations as well as hyperparameters like step size of gradient descent during the learning process.
The image quality parameters of the DIP output were evaluated after each iteration. For Shape phantom data, a total of 500 iterations of the DIP learning process were performed, and for Resolution phantom data, a total of 4200 iterations were performed. Both normalized and non-normalized ("whitened") data were used for preprocessing, as well as signal to noise thresholding $\tau \in \{0, 1, 5\}$.
It can be seen (cf. Fig. 4.7) that the results of all data used converge with increasing iteration. However, the value against which the values converge is different.
Results of the Shape phantom converge within fewer iterations than those of the Resolution phantom. In particular, in the case of $\mathrm{SSIM}_{\mathrm{max}}$, it can be seen that after about 100 to 200 iterations, the value increases very little. In contrast, $\mathrm{SSIM}_{\mathrm{max}}$ for the Resolution phantom results still increases strongly after 500 iterations in many cases. In the results of both phantoms, there are individual combinations of hyperparameters and preprocessing steps, in which the value of the image quality parameters increases abruptly at the beginning and stagnates at a level. All in all, this level is lower than the image quality parameter, which is reached with a slow increase after several iterations. In the image this is reflected as a constant output. Thus, these results are unsuitable.
Over many iterations converging results of the Resolution phantom achieve a higher $\mathrm{PSNR}_{\mathrm{max}}$ compared to the Shape phantom (cf. Fig. 4.7). However, $\mathrm{SSIM}_{\mathrm{max}}$ with a best level of about 0.35 is significantly lower than the results of the Shape phantom with an achieved $\mathrm{SSIM}_{\mathrm{max}}$ of about 0.9. Thus, differences in the performance of the DIP are evident for different scanned phantoms.

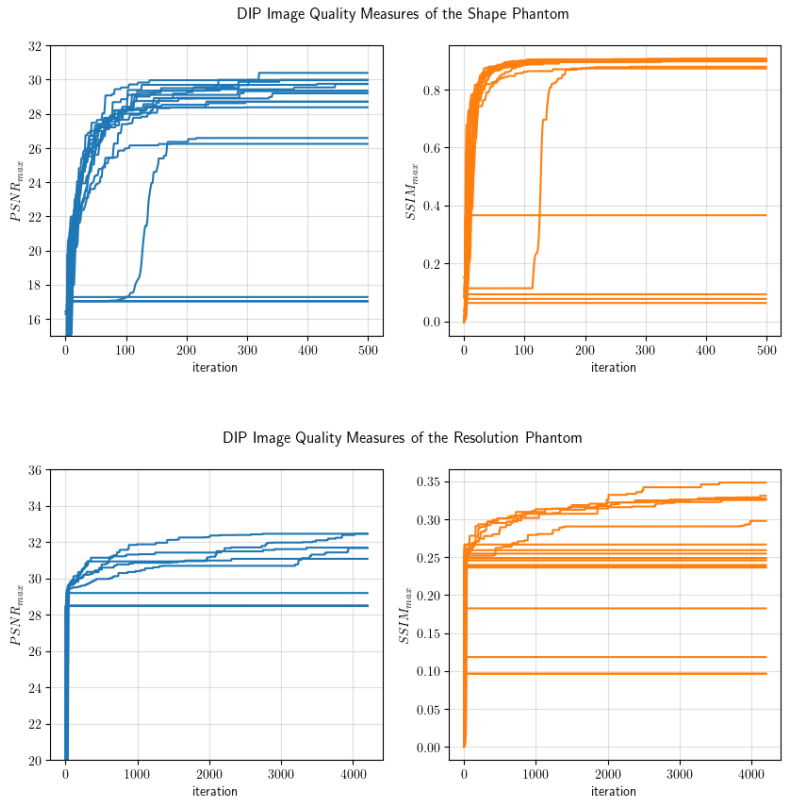

Figure 4.7: *Image quality measures* PSNR_{max} *(blue) and* SSIM_{max} *(orange) of DIP results over learning iterations using different preprocessed data.* Image qualty measures of the Shape phantom are shown in the top row, results of the Resolution phantom in the bottom row.

The influence of different hyperparameters on the image quality of the reconstructed concentration distribution is analyzed. The selected step size is relevant for the convergence behavior of the method DIP. In Figure 4.8 the course of SSIM_{max} over several training iterations is shown. A distinction is made between the Shape phantom (top row) and the Resolution phantom (bottom row). Based on the used hyperparameters 10^{-4}, 10^{-3} and 0.01 (left to right) the results are plotted separately. At the smallest chosen step size, most results of differentially preprocessed data converge towards a high threshold. In contrast, with a large step size 0.01, the effect of rapid increase and stagnation at low level often occurs. Thus, the selected step size seems to correlate with the highest SSIM_{max} achieved.
Especially noticable is this effect at the results of the Resolution phantom (cf. Fig. 4.8, bottom row). A step size 0.01 set leads to a rapid increase in the first iterations and stagnation during higher iterations. This happens for every preprocessed data set of Resolution phantom measurements. The highest SSIM_{max} is 0.27 which is below the best overall result 0.35 of the Resolution phantom. This indicates that a smaller step width 10^{-4} or 10^{-3} is more suitable for better image quality, especially in case of the Resolution phantom.
The difference between Shape and Resolution phantom may lie in the nature of the phantom design: The Shape phantom consists of rather large,

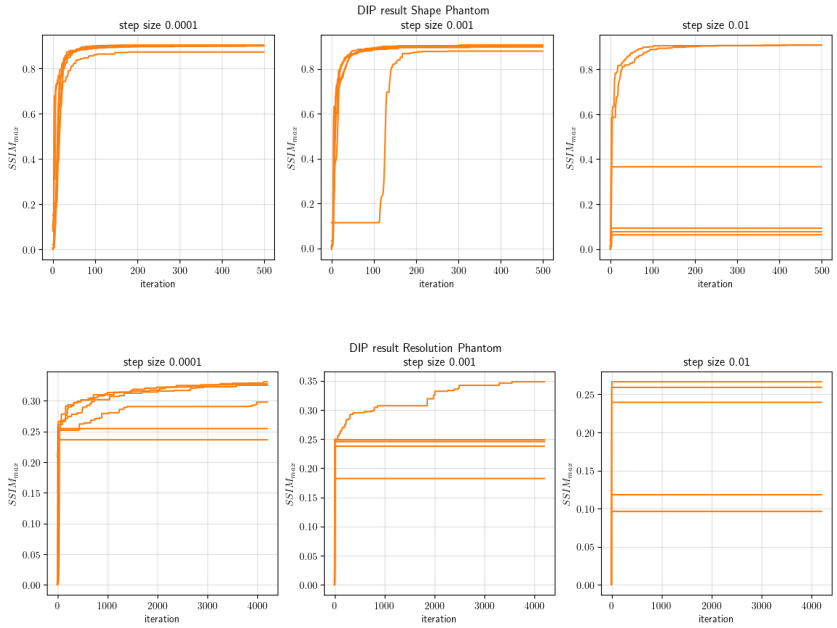

Figure 4.8: *$SSIM_{max}$ of different preprocessed data using DIP split according to the step size used.* Image quality measure SSIM_{max} of different preprocessed data using DIP. The result is split according to the chosen step size 10^{-4}, 10^{-3}, 10^{-2} (left to right) during reconstruction and phantom data (top Shape phantom, bottom Resolution phantom).

contiguous areas in the layers. This corresponds to a high proportion of low frequencies in the image. Sharp edges at the edge of the Shape phantom are high frequent. Since the Resolution phantom consists of thin, filled tubes, the area to be displayed is much smaller and not as contiguous as in the Shape phantom. Thus, the low-frequency portion of the phantom to be displayed is lower than compared to the Shape phantom. Finally, the observation as in [UVL20] shows that high-frequency parts are reconstructed only in higher iterations with DIP. Thus, a high number of iterations as well as rather smaller step size are suitable if the SPIO distribution of the scan object is expected to be rather sparse.

In order to analyze the influence of training iterations, the image quality measures are analyzed over a large number of iterations and different data. To show the observed behavior in the following figures of this section, normalized data of the Shape phantom with $\tau = 5$ SNR-thresholding were used for the DIP training with step size 0.001.

The image quality measures SSIM_{max} and PSNR_{max} are shown in Fig. 4.9. During the first 350 iterations, both image quality measures increase strongly on average. With increasing training iterations, the image quality measures decrease.

With the decrease in image quality parameters, the effect of overfitting is visible in the resulting images cf. Fig. 4.9. In addition to that, the property of DIP described in the original paper [UVL20] of reconstructing low frequent parts of an image first is also observed for MPI reconstruction. This is shown

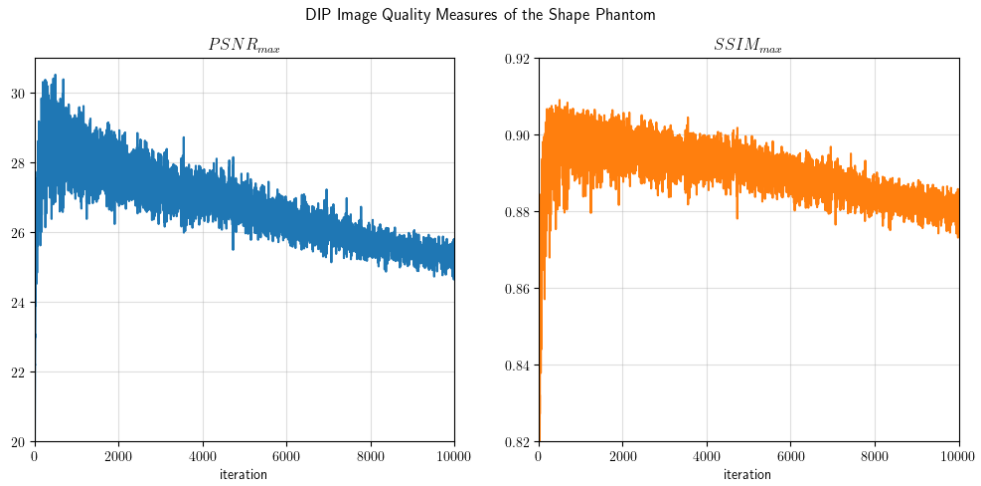

Figure 4.9: *Image quality measures $PSNR_{max}$ and $SSIM_{max}$ over a large number of iterations.* Normalized data of the Shape phantom with SNR-thresholding $\tau = 5$ and step size 0.001 were used for the DIP approach.

in Figure 4.10 and Figure 4.11, where the middle slices of the Shape phantom reconstruction are displayed at different training iterations of DIP. After the first two iterations, the output looks randomly computed without reference to the original phantom. At 20 iterations, low frequent parts are shown. To be more precise, the overall shape is formed and shown in the image. After further iterations the shapes are more formed and displayed until a good image quality is reached at around 300 iterations. Large numbers of iterations 1000, 5000 and 10000 lead to noise-like artifacts in the area of the phantom. These artifacts become stronger the higher the number of iteration is.
To conclude, early stopping of the DIP training process after a phantom-dependent iteration leads to a better image quality. The tradeoff between underfitting and overfitting is strongly influenced by the chosen number of training iterations.

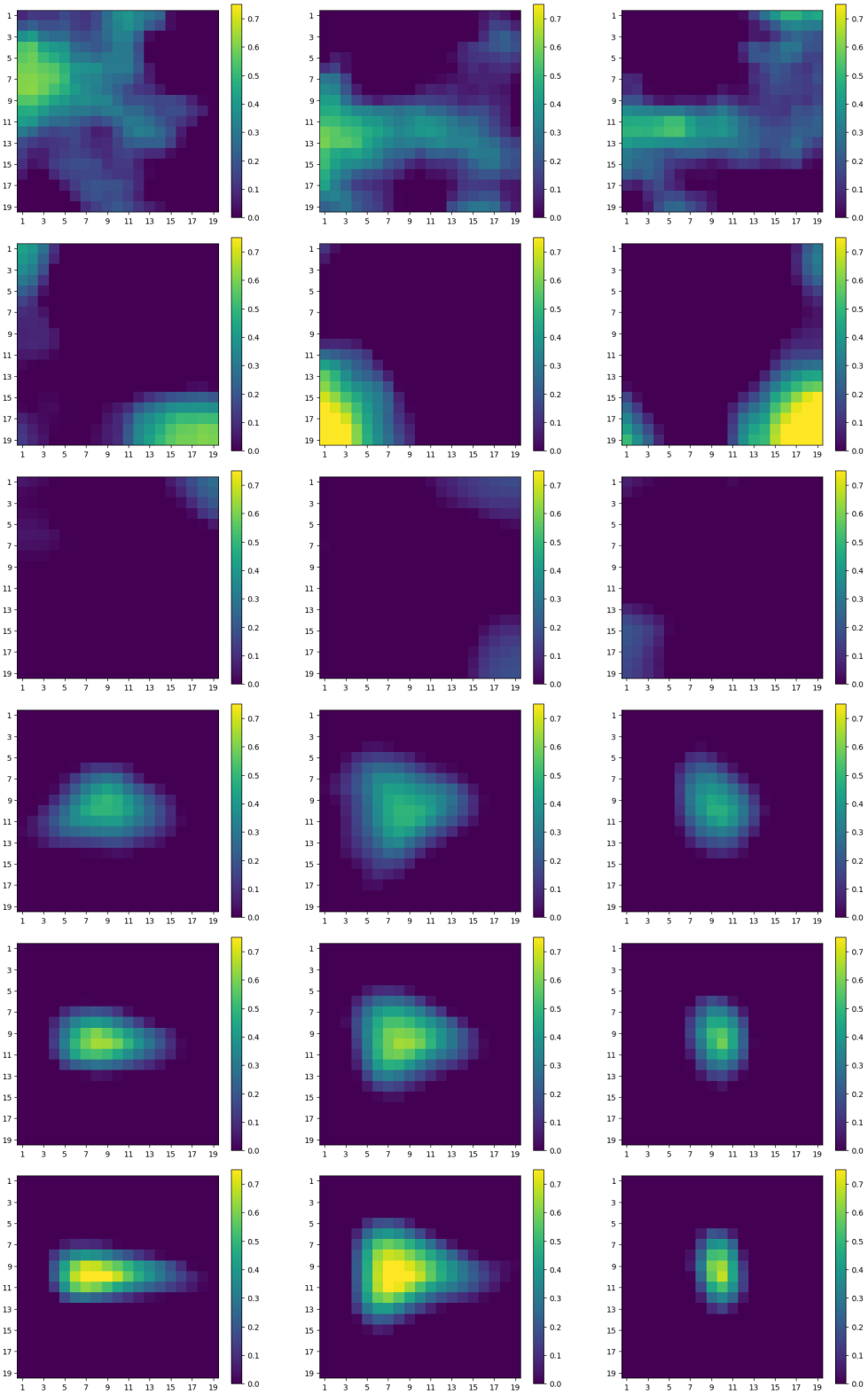

Figure 4.10: *DIP result of the Shape phantom, with step size* 10^{-3} *after different iterations.* Number of iterations from top to bottom: 1, 2, 5, 20, 30, 40.

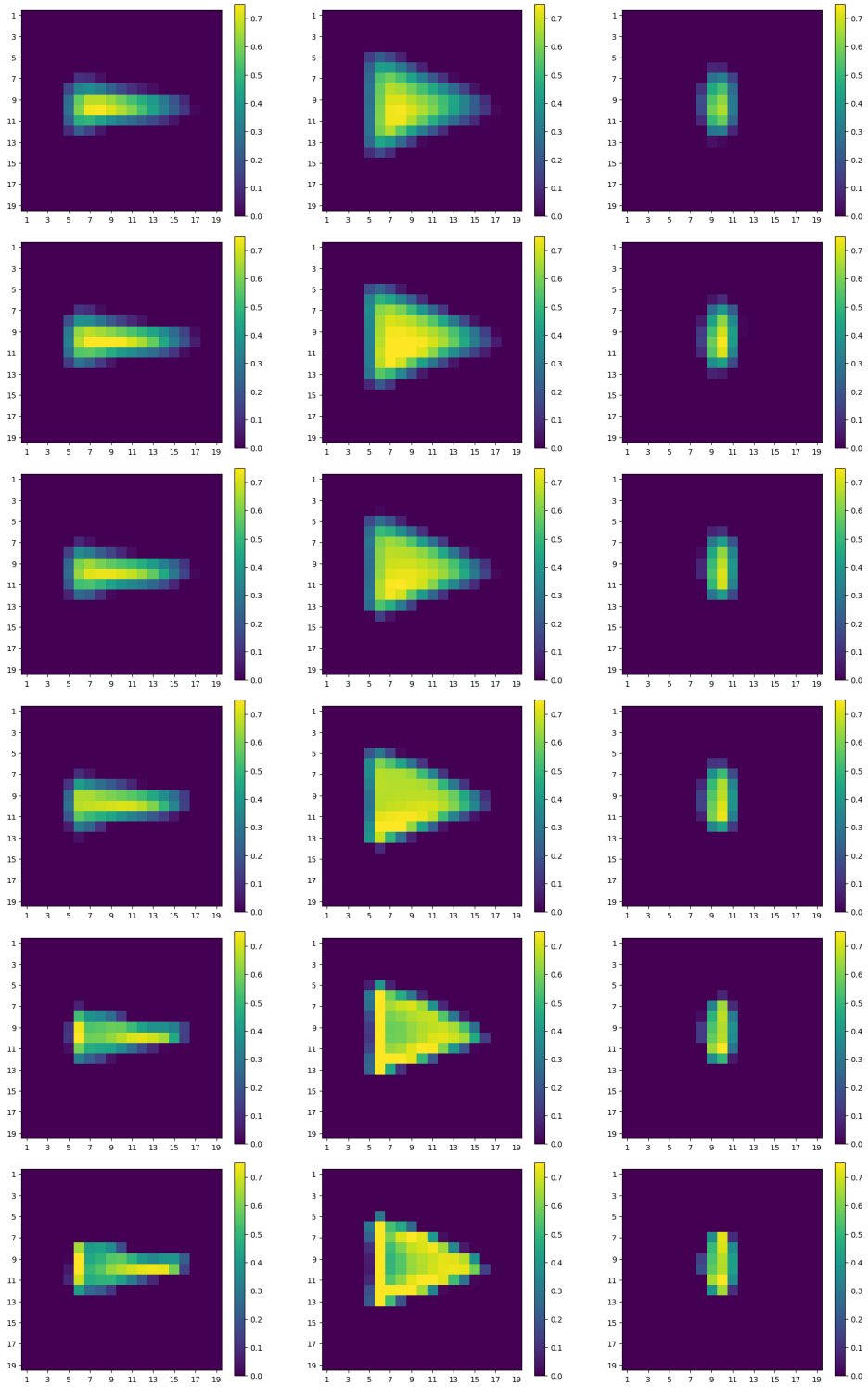

Figure 4.11: *DIP result of the Shape phantom, with step size* 10^{-3} *after different iterations.* Number of iterations from top to bottom: 100, 200, 300, 1000, 5000, 10000.

4.4 PLUG AND PLAY PRIOR (PNP)

PnP iterates between reconstruction and denoiser. In the following section, the results of the denoised reconstruction is analyzed.

4.4.1 *Choice of the axis along which the reconstructed volume is sliced*

In order to denoise 2D images, the axis along which the reconstructed volume is sliced into 19 images has to be chosen. Two different approaches were tested: At the first approach, an axis is chosen randomly at each iteration. The second approach slices the volume always along the same axis, which is set to x-axis in the further experiments .
The image quality measures for one preprocessed Shape phantom dataset but different hyperparameters are shown in Fig. 4.12. In the left column, results of the randomly chosen axis are shown, in the right column results of a set axis are visualized. The plot of the quality measures produced by PnP with a set axis are smoother. In the first few iterations, the overall level of the image quality measures is comparable. Especially with an increasing number of iterations, both PSNR_{max} and SSIM_{max} are lower for a set choice compared to a random choice of slicing axis. The few starting points at the first iteration are discussed by evaluating Fig. 4.16 in Chapter 4.4.2.
The differences in the reconstructed images at iterations 10 (top row) and 39 (bottom row) between PnP results choosing a randomis slicing axis (left three images) compared to a set slicing axis (right three images) are shown in Fig. 4.13. Both reconstructions are similar at iteration 10, although a darker line is visible in the reconstruction using a set axis. This artifact gets worse with a larger iteration: At 39 iterations, the line artifact is prominent in the XZ-plane and YZ-plane. The triangle in the XY-plane is heavily corrupted. In contrast to that, the reconstruction at the same iteration and hyperparameters, with the exception of a random choice of sliced axis, does not show this artifact. The visual impression became worse compared to smaller iterations but not as strong as the reconstruction with a set axis.
Since experiments have shown that a choice of a random axis to slice the cube into images leads to better image quality compared to always slicing along the same axis. For that reason, a random axis is always chosen in order to compute the following results.

4.4.2 *Hyperparameters*

In order to find the best results of PnP, different hyperparameters were tuned:

- $\alpha_{start} \in \{10^{-2}, 10^{-3}, 10^{-4}, 10^{-5}\}$,
- $\alpha_{incr} \in \{10^{-3}, 10^{-4}, 10^{-5}\}$,
- $\lambda\sigma^2 \in \{10^{-6}, 10^{-7}, 10^{-8}, 10^{-9}, 10^{-10}\}$.

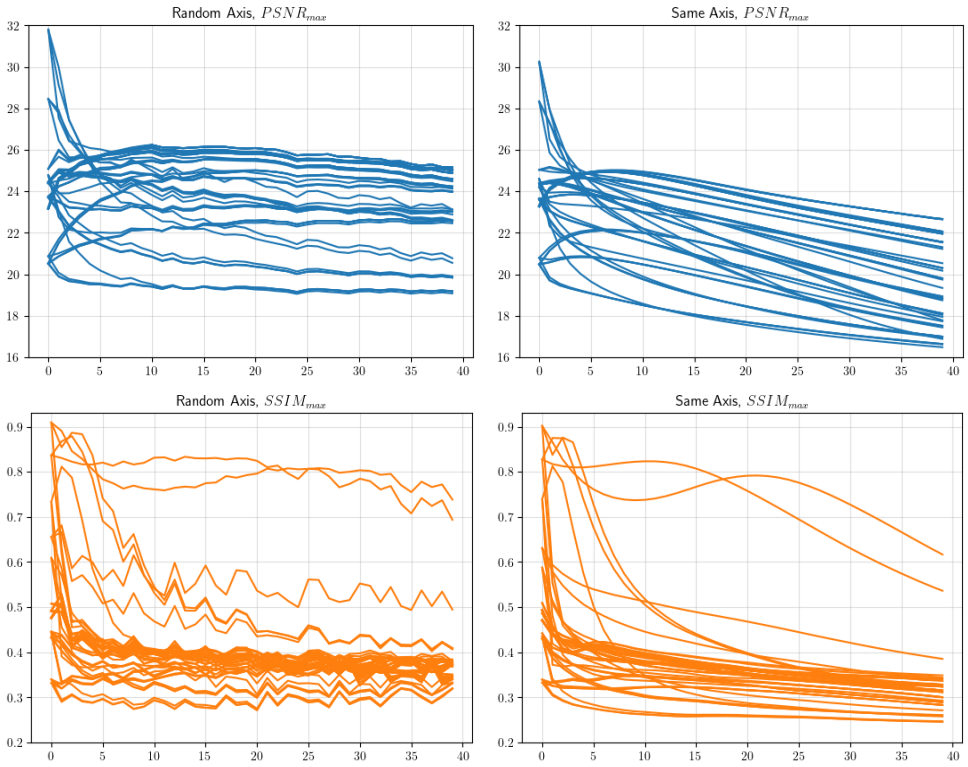

Figure 4.12: *$PSNR_{max}$ and $SSIM_{max}$ of the PnP approach using different slicing methods.* Results of normalized, $\tau = 1$ SNR thresholded Shape phantom data are shown. Left: A random axis is chosen to slice the volume at each iteration. Right: X-axis is chosen to slice the volume at each iteration.

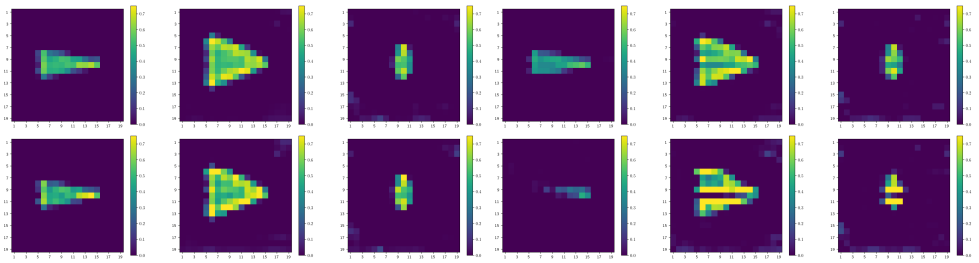

Figure 4.13: *Shape phantom reconstructions of PnP applying random vs. set chosen slicing axis.* All three planes are shown so that the three images belong together. Top left: random choice iteration 10, top right: set axis iteration 10, bottom left: random choice iteration 39, bottom right: set axis iteration 39 The same hyperparameters $\alpha_{start} = 10^{-5}, \alpha_{incr} = 10^{-4}, \lambda\sigma^2 = 10^{-6}$ were used for the reconstruction.

All preprocessed data sets consisting of normalized and not normalized Shape phantom and Resolution phantom data with applied SNR thresholds $\tau \in \{0, 3, 5\}$ were evaluated.
The image quality measures of the reconstruced normalized Resolution phantom data with SNR threshold $\tau = 1$ are shown in Fig. 4.14. Whereas SSIM_{max} increases with higher iterations, PSNR_{max} decreases in most cases over time. Compared to the results of the Shape phantom, SSIM_{max} is generally lower

with a difference of around 0.5. Based on the visual impression, the Resolution phantom results are therefore expected to be worse compared to the Shape phantom results. An example with decreasing $\mathrm{PSNR}_{\mathrm{max}}$ and in-

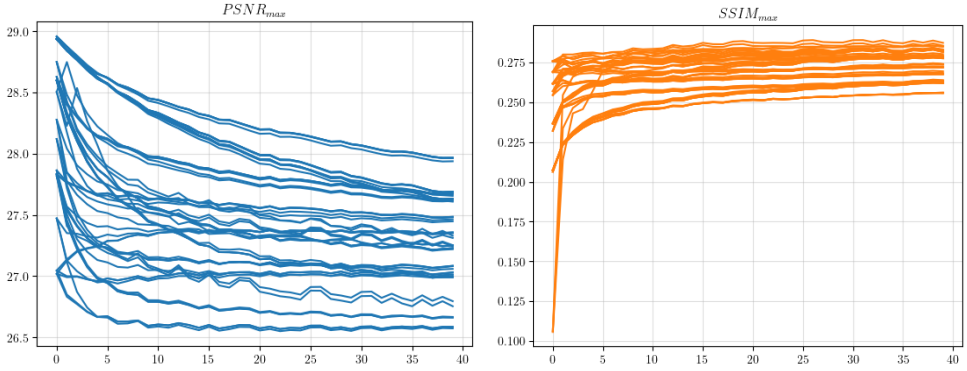

Figure 4.14: *$PSNR_{max}$ and $SSIM_{max}$ of Resolution phantom reconstructions using PnP.* Normalized, $\tau = 1$ SNR thresholded Resolution phantom data and different hyperparameters are used.

creasing $\mathrm{SSIM}_{\mathrm{max}}$ is visualized in Fig. 4.15. The corresponding reconstructed concentration distribution of the middle slices after the first iteration (middle) and iteration 40 (bottom) are also shown. The result at the first iteration inherits high $\mathrm{PSNR}_{\mathrm{max}}$ and rather low $\mathrm{SSIM}_{\mathrm{max}}$, whereas the result at iteration 40 has lower $\mathrm{PSNR}_{\mathrm{max}}$ and higher $\mathrm{SSIM}_{\mathrm{max}}$. By comparing the results visually, the reconstructed concentration distribution in the first iteration is more blurry. This can be perceived especially at the XZ-plane, where the tubes are sliced in order to gain information about the resolution. The tubes can be distuingished better at reconstruction after iteration 40 with higher $\mathrm{SSIM}_{\mathrm{max}}$ although they are not perfectly separated.
In contrast to the Resolution phantom's results, the results of the Shape phantom differ especially by comparing $\mathrm{PSNR}_{\mathrm{max}}$ and $\mathrm{SSIM}_{\mathrm{max}}$. Image quality measures of reconstructions using PnP of normalized, $\tau = 1$ SNR thresholded Shape phantom data are shown in Fig. 4.16. Most often, $\mathrm{SSIM}_{\mathrm{max}}$ values decrease after the first few iterations. For some hyperparameters, the image quality measure is generally low showing that the choice of hyperparameters is non-trivial for the quality of the output. Hyperparameters α_{start} and $\lambda\sigma^2$ influence the first output of the denoised result. This is the reason for the few origins of the image quality measurements in the Figure. The highest start of $\mathrm{PSNR}_{\mathrm{max}}$ is generated by $\alpha_{start} = 10^{-5}$ and $\lambda\sigma^2 = 10^{-6}$.

In some cases, the image quality measures are very high in the first denoised output of PnP and decrease with further iterations. An example for that is shown in Fig. 4.17, where non-normalized data with SNR-threshold $\tau = 1$ data of the Shape phantom is reconstructed with PnP. The result of the first denoising iteration shows a reconstruced concentration distribution that is homogeneous in the center of the shape. The overall brightness fits the linearity assumption. Edges are sharp and the images are nearly free of noise. Some low-level noise is visible in the background area of the shown YZ-plane displaying the elliptic shape. After completing 40 iterations, the

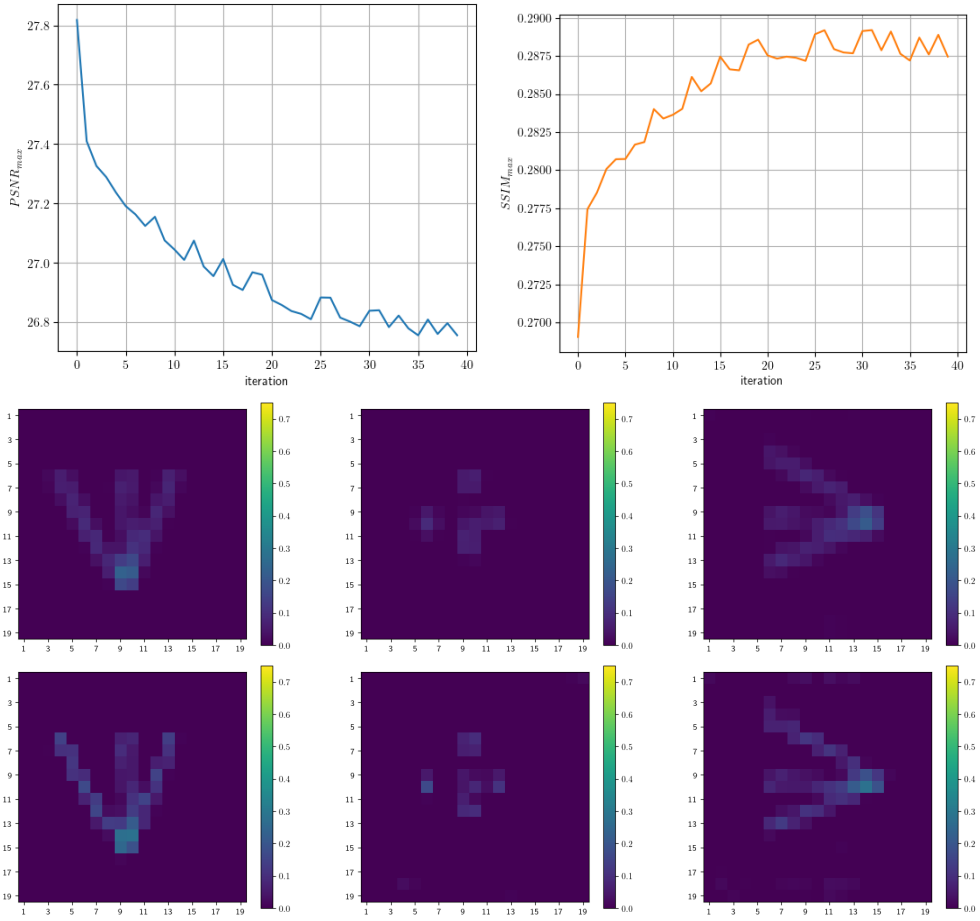

Figure 4.15: *Reconstruction of Resolution phantom data at different iterations of the PnP method.* Image quality measures PSNR_{max} and SSIM_{max} (top) of normalized, $\tau = 1$ SNR thresholded Resolution phantom data are shown. The corresponding reconstruction after iteration 0 (middle) and iteration 39 (bottom) are displayed. Used hyperparameters are $\alpha_{start} = \alpha_{incr} = 10^{-5}$, $\lambda\sigma^2 = 10^{-7}$.

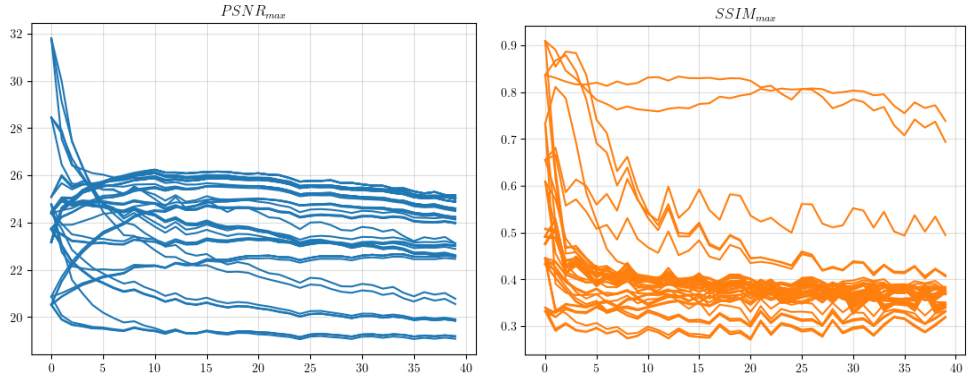

Figure 4.16: *$PSNR_{max}$ and $SSIM_{max}$ of Shape phantom data reconstructions at different PnP iterations.* Normalized, $\tau = 1$ SNR thresholded Shape phantom data and different hyperparameters are evaluated.

visual impression fits the decreased image quality measures: Some noise is shown in the background but moreover, the shapes now seem noisy and the uniform concentration level is lost and does not look denoised.

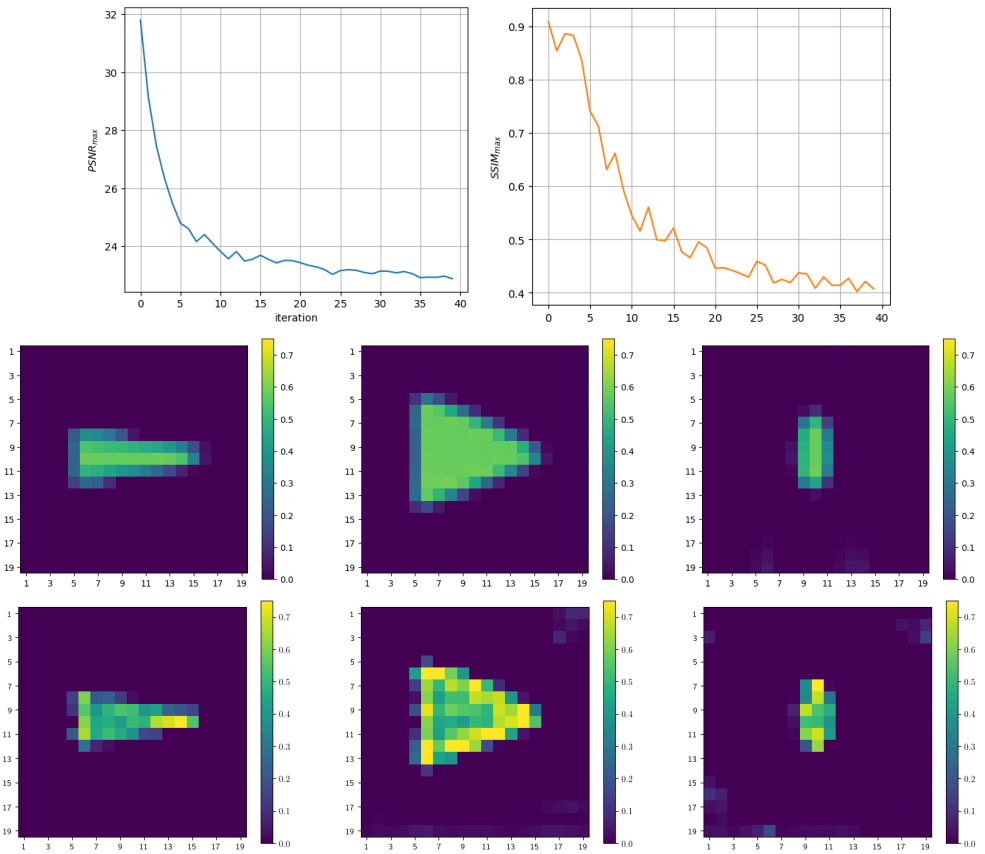

Figure 4.17: *Example of high image quality after the first iteration of the PnP result (middle) vs. low image quality after* 40 *iterations (bottom).* The Image Quality Measures of the preprocessed data set and hyperparameters used are shown in the top row. Data used: Shape phantom using normalization and SNR threshold $\tau = 1$, hyperparameters $\alpha_{start} = 10^{-5}$, $\alpha_{incr} = 10^{-5}$ and $\lambda\sigma^2 = 10^{-6}$

4.5 COMPARISON OF THE DIFFERENT RESULTS

The highest image quality measures of the preprocessed MPI data with SNR-filtering using thresholds $\tau \in \{0, 1, 5\}$ are shown in the following tables. There is a different table for each of the scanned phantoms, Shape phantom and Resolution phantom, as well as whether the preprocessing step normalization was applied.
An overview of the corresponding hyperparameters is given in the appendix. The first two Tables 4.1 and 4.2 show the results of preprocessed Shape phantom data. Implemented Tikhonov Regularization leads in all 6 preprocessed data sets to the lowest image quality measures, both PSNR_{max} and SSIM_{max}. PnP has highest PSNR_{max} with preprocessed data using rather low SNR thresholds $\tau \in \{0, 1\}$. Compared to that, preprocessed data with $\tau = 5$ performs worse. SSIM_{max} values of Tikhonov Regularization are at least 0.5 lower compared to the results of the Learning-based techniques.

Shape Phantom	PSNR_{max}			SSIM_{max}		
Regularization Technique	$\tau = 0$	$\tau = 1$	$\tau = 5$	$\tau = 0$	$\tau = 1$	$\tau = 5$
Tikhonov Regularization	22.28	22.38	22.64	0.32	0.32	0.39
DIP	26.75	29.35	<u>30.39</u>	0.88	<u>0.90</u>	<u>0.91</u>
PnP	<u>30.30</u>	<u>30.10</u>	25.78	<u>0.90</u>	<u>0.90</u>	0.85

Table 4.1: Best image quality measures of the Shape phantom reconstruction using different Regularization techniques split according to SNR-filtering with threshold τ during preprocessing. Data were preprocessed without Normalization. The highest values of each preprocessed data set are underlined.

Shape Phantom	PSNR_{max}			SSIM_{max}		
Regularization Technique	$\tau = 0$	$\tau = 1$	$\tau = 5$	$\tau = 0$	$\tau = 1$	$\tau = 5$
Tikhonov Regularization	22.86	23.09	23.01	0.33	0.34	0.36
DIP	28.70	29.75	<u>29.98</u>	0.90	<u>0.91</u>	<u>0.91</u>
PnP	<u>30.86</u>	<u>31.80</u>	26.24	<u>0.91</u>	0.90	0.86

Table 4.2: Best image quality measures of the Shape Phantom reconstruction using different Regularization techniques split according to SNR-filtering with threshold τ during preprocessing. Data were preprocessed with Normalization. The highest values of each preprocessed data set are underlined.

Tables 4.3 and 4.4 show the best image quality measures of preprocessed Resolution phantom data. In 5 of 6 preprocessed data sets, Tikhonov regularization achieves highest SSIM_{max}. Considering PSNR_{max}, DIP achieves the highest values in 5 of 6 preprocessed data sets of the Resolution phantom.

Compared to the results of Shape phantom, the $SSIM_{max}$ of the Learning-based regularization techniques is significantly lower.

Resolution Phantom	$PSNR_{max}$			$SSIM_{max}$		
Regularization Technique	$\tau = 0$	$\tau = 1$	$\tau = 5$	$\tau = 0$	$\tau = 1$	$\tau = 5$
Tikhonov Regularization	29.98	30.28	30.03	<u>0.33</u>	0.27	<u>0.33</u>
DIP	<u>31.67</u>	<u>32.45</u>	<u>31.07</u>	0.30	<u>0.32</u>	<u>0.33</u>
PnP	29.06	29.02	29.02	0.27	0.28	0.29

Table 4.3: Best image quality measures of the Resolution Phantom reconstruction using different Regularization techniques split according to SNR-filtering with threshold τ during preprocessing. Data were preprocessed without Normalization. The highest values of each preprocessed data set are underlined.

Resolution Phantom	$PSNR_{max}$			$SSIM_{max}$		
Regularization Technique	$\tau = 0$	$\tau = 1$	$\tau = 5$	$\tau = 0$	$\tau = 1$	$\tau = 5$
Tikhonov Regularization	30.23	<u>30.24</u>	30.23	<u>0.38</u>	<u>0.37</u>	<u>0.39</u>
DIP	<u>31.69</u>	28.48	<u>32.45</u>	0.33	0.25	0.35
PnP	29.02	28.96	30.00	0.28	0.29	0.30

Table 4.4: Best image quality measures of the Resolution Phantom reconstruction using different Regularization techniques split according to SNR-filtering with threshold τ during preprocessing. Data were preprocessed with Normalization. The highest values of each preprocessed data set are underlined.

5 DISCUSSION

The results of this thesis include image quality measures of Tikhonov Regularization, Deep Image Prior and Plug and Play Prior using a CNN denoiser. These results are further inspected and the methods critically discussed. Furthermore, possible approaches to resolve challenges encountered are identified.

5.1 DATA AND PREPROCESSING

MPI is an emerging imaging modality which is in a preclinical development phase. There are only few publicly available data which limits the possibilities for transfer learning without overfitting the few available datasets. For that reason, no transfer learning was performed. Moreover, transfer learning is often not wanted in the medical field since artifacts like hallucination should be avoided since a wrong diagnosis can have severe consequences for a patient. Other MPI data can be used and reconstructed with the proposed regularization techniques since overfitting is unlikely due to the fact that hyperparameters need to be chosen for each newly introduced dataset and thus the results are not influenced by pretrained supervised algorithms. On the other hand, computationally intensive hyperparametertuning will be needed for each data set reconstructed.
There are publications in which preprocessed MPI data are used in order to reconstruct concentration distributions but no preprocessing toolbox is publicly available. For that reason, preprocessing steps were implemented in Matlab. Since only few data were used in the course of this thesis, the performance of applied preprocessing steps is not proven for MPI data in general. If more data are available, preprocessing steps can be enhanced like taking covariance into account in the data normalization step.
There are already more advanced MPI scanners [TG20] compared to the one used for the freely accessible data acquisition. Since these are the only freely accessible data as of my current knowledge, the data used are still considered state of the art.
The calibration data of the dataset are already Fourier Transformed which forces the user to work with Fourier Transformed data. Although an inverse Fourier Transformation could be applied, original time series data are not retrieved since they are averaged.

5.2 TIKHONOV REGULARIZATION

The implemented Standard L^2-Tikhonov Regularization leads to reconstructions on which the scanned phantoms can be recognized. It is shown that the regularization parameter α controls the tradeoff between low frequent parts of an image like large bright or dark areas and high frequent parts like edges and noise. The approach is simply implemented and computated fast. Compared to the Learning-based regularization techniques, the implemented Tikhonov Regularization performs worst reconstructing the shape phantom according to the image quality measures. SSIM_{max} of the reconstructed Resolution phantom data is highest with an applied L^2-Tikhonov Regularization. This shows that Learning-based methods do not generally outperform standard regularization techniques.
In order to improve the results using Tikhonov Regularization, further constraints and terms can be added to the Tikhonov functional. Total Variation (TV)-regularization might lead to better results [Dit+].

5.3 DIP

Compared to the implemented Tikhonov Regularization, the DIP results of the Shape Phantom are better according to the used image quality measures. Edges are preserved while keeping the noise level low.
Early stopping is necessary in order to achieve a good image quality. Otherwise, noise in the scan data is also reconstructed in the result. Especially due to the hyperparametertuning and the iterations used for the training process, the computation time for MPI reconstruction is higher than the implemented Tikhonov Regularization. On top of that, more computation resources are needed in order to store and apply the used CNN. The higher demand for computation resources and time is challenging in a real-world scenario in the medical field where resources are often limited.
Another disadvantage of DIP and its application in a real-world scenario is the problem of a missing ground truth. Usually, subjects and objects are scanned without knowing the real concentration distribution of a tracer. Moreover, the subject or object is scanned because the concentration distribution is of interest and should be detected with MPI. Since there is no ground truth of the concentration distribution, image quality measures like $SSIM$ and $PSNR$ can not be computed in order to identify the best reconstruction and suitable hyperparameters including number of iterations. It is shown in the course of the thesis that the number of best iterations varies depending on the scanned phantom itself. A proposition for a good amount of iterations can thus not be given when scanning an unknown object. A visual inspection of each iteration output is also not suitable for the application in the medical field. Nonetheless, a tuning will be necessary for each new scan which can be computationally challenging.
The different needed step size and number of learning iterations of Shape phantom compared to the Resolution phantom could be explained by the

characteristic form of the phantoms. The shape phantom consists of large areas which have the same concentration. This means the proportion of high frequent parts in the image is rather high compared to the Resolution phantom consisting of thin tubes. In order to achieve a finer distinction between noise and small structure of the Resolution phantom, smaller step sizes therefore could be useful.

5.4 PNP

In order to denoise the volume with a 2D denoiser CNN, it is sliced along an axis in 19 images that are denoised separately. The choice of this axis has an influence on the reconstructed volume. It is shown that strong line artifacts are visible in the reconstruction using always the same axis to slice the volume. These artifacts do not appear if the axis is chosen randomly. This phenomenon might be caused by the independent treatment of the sliced images although a dependency exists in the neighborhood in all 3 dimensions. Followingly, it is important to randomize the choice of an axis at each iteration. In future works, a 3D denoisier CNN can be implemented and tested. Since 3D convolution kernels are used, the dependency of close neighborhood of each voxel is taken into account and could improve the results.
Resolution phantom and Shape phantom differ in the number of iterations needed to achieve a high SSIM_{max}. Many iterations are better in case of the Resolution phantom whereas the Shape phantom reaches the best SSIM_{max} after few iterations. This can be have different causes: On the one hand, chosen hyperparameters for the Shape phantom might not be very suitable and could be tuned better if more time was invested. The example of a high achieved image quality of the Shape phantom as in Fig. 4.17 contradicts this hypothesis. Another reason for the different number of iterations needed could be similar to DIP: Since the shape phantom consists of a higher portion of low frequencies, it is reconstructed faster and therefore a stronger denoising possible without losing information of the Phantom.
Another explanation for the few iterations needed in order to achieve high image quality measures is the size of denoised images. With 19×19, the size of denoised images is smaller than originally intended. Padding and therefore increasing the size was needed in order to fit the images to the used network. Since the images are way smaller, denoising could be achieved in the course of fewer iterations.
In order to analyze the results being more physically acurate and achieve better results according to image quality measures, negative values can be set to 0. This was not applied in this work since the raw output of the Denoiser was of interest.
The used denoisier CNN is trained for input with Gaussian noise. Noise of MPI scan data is not proven to be Gaussian. Moreover, there are several noise sources of MPI that are not necessarily Gaussian. Examples are random processes inside the device like thermal noise of receive coils, harmonic interference from non-linear electronic components or abrupt signal changes

or distortions that can be caused by the electrical discharge of a hardware component or malfunction in the data acquisition chain [PTH23],[Pay+20]. For these reasons, non-gaussian noise proportion of MPI scan data noise is not quite suitable for gaussian denoising. To overcome this problem, transfer learning with lots of MPI or MRA data could be tested in future work if transfer learning and the possibility of hallucination artifacts are accepted. Another method to tackle this problem is enforcing denoising constraints like sparsity in the reconstruction part of PnP.

5.5 OUTLOOK

To improve the performance of the PnP approach with a learned denoiser, transfer learning with MPI data or estimation of noise in MPI could lead to better results.
Standard methods of supervised machine learning like transfer learning could not be applied due to the lack of freely accessible data. In a future work in order to tune a denoising network, simulated data [Zha+23a] [NK23] or similar data to MPI, like experimental magnetic resonance angiogram (MRA) images [Ask+22], could be used. Pre-condition for that is the accessibility of a simulator, scan data or reconstructed images. Reconstructed clinical images are often not freely accessible due to patient information restrictions. So it is especially challenging to access a massive amount of scan data and actual concentration distribution pairs.
Another possibility is the usage of a CNN suitable for 3D input. The importance of considering the dependency of voxels in the neighborhood was shown by different choices of an axis along which the volume was sliced for 2D denoising. Therefore, a 3D denoiser network could improve the results.
In order to tackle the problem of the missing ground truth data and following problem of choosing the best hyperparameters, a deep learning-based postprocessing technique which tries to choose the best hyperparameters can be tested [KJG23].
The measurement-based approach main disadvantage is the time-consuming calibration time and the need to recalibrate if the scan setup changes. Although there are propositions to reduce the calibration time [Gla+20], a model-based approach does not lack from these disadvantage and might lead to better results. Furthermore, in the measurement-based approach the SM has to be explicitly set up and stored in memory beforehand, which is memory consuming. Moreover, large SM can lead to long reconstruction times [Zha+23a].
In this thesis, data with only one type of tracer was used. In future works, scans with different tracers could be simulated in order to create color Magnetic Particle Imaging (cMPI) [Rah+15] [Zha+23b]. The performance of the proposed regularization techniques can be evaluated using such data.

6 CONCLUSION

Real MPI data from a preclinical scanner were preprocessed.
Tikhonov regularization and Learning-based techniques Deep Image Prior and Plug and Play framework with a pretrained gaussian denoiser were applied to MPI scan data. Hyperparameters were finetuned and the results evaluated by standard image quality measures Peak Signal to Noise Ratio and Structural Similarity. In addition to that, uncertainty of phantom positions were taken into account in the calculation of the image quality measures.
In summary there are multiple main findings resulting from the quantitative evaluation of the discrete concentration distributions of the different regularization techniques: The implemented Tikhonov regularization leads to visually good results and was easily implemented. Both the shapes of Shape phantom and Resolution phantom are perceived. Compared to the Learning-based methods, the implemented Tikhonov regularization performed in many cases better in the reconstruction of Resolution phantom data and worse in the reconstruction of Shape phantom data considering image quality measures $\mathrm{PSNR}_{\mathrm{max}}$ and $\mathrm{SSIM}_{\mathrm{max}}$ of the reconstructed concentration distribution. It is shown that the regularization parameter α in Tikhonov regularization controls the tradeoff between the lower frequent and higher frequent parts of the reconstruction. If chosen too high, the images appear blurry especially in edge-regions of a phantom meaning the high frequent parts of the images are too strongly regularized. If the regularization parameter is too small, edges are preserved but noise is also enhanced. If the regularization term is weighted too little, noise artifacts appear in the reconstructed images.
Compared to the Shape phantom results of the implemented Tikhonov regularization, the DIP results perform better according to the image quality measures and visual impression. Edges are better preserved in the best DIP reconstruction while less noise is seen in the result.
The reconstructions of MPI data via DIP strongly depend on the chosen hyperparameters and seeds. Some hyperparameters lead to not useful reconstructions, where the output is constant and no concentration distribution is seen. It is shown that the number of used iterations in order to achieve the best results with regards to image quality measures differs from the scanned phantom, which makes finding the best choice challenging for an application in a real-world scenario scanning an unknown object. Another challenge of the application of DIP in a clinical area are limited computation resources. DIP takes more computation time and resources than the implemented Tikhonov L^2-Regularization. On top of that, many iterations and hyperparameters need to be computed and compared in order to identify the "best" reconstruction.

The results of PnP strongly vary by the choice of hyperparameters.
Since a pretrained 2D denoiser CNN was used, different slicing methods of the reconstructed volume in order to denoise it in 2D were tested. Slicing the volume into single images was implemented in two different ways: The first option was the choice of the same axis at each iteration, which lead to line artifacts in the reconstruction. The second option of choosing a random axis to slice the volume into images leads to better results. The visually best reconstruction of the Shape phantom was achieved by the PnP method.
The goal of the thesis was overall reached by understanding and preprocessing existing MPI data and implementing, tuning and evaluating different regularization techniques.
With more time invested in noise estimation of MPI data and finetuning of hyperparameters of the PnP framework, better results might be achievable. Due to the flexibility of the PnP framework, there is a high potential to achieve better results by plugging in other solvers like ADMM or use a more suitable denoiser network.
Promising future research areas are the identification and description of MPI noise. Knowledge about the noise and noise structure in MPI can be incorporated in the PnP denoiser network's noise level map. This holds potential to increase the quality of the PnP results using a denoiser network. Furthermore, transfer learning of similar imaging modalities can be performed like experimental Magnetic Resonance Angiogram (MRA) images [Ask+22], which have shown promising results.
Another promising research area is the model-based MPI approach which does not need the time consuming calibration process of scanning many positions of a reference "Delta" Sample.

A

APPENDIX

A.1 HYPERPARAMETERS OF THE REGULARIZATION TECHNIQUES LEADING TO HIGHEST IMAGE QUALITY MEASURES

α	$PSNR_{max}$			$SSIM_{max}$		
Data	$\tau = 0$	$\tau = 1$	$\tau = 5$	$\tau = 0$	$\tau = 1$	$\tau = 5$
Shape, not normalized	10^{-4}	$5 \cdot 10^{-4}$	0.001	$5 \cdot 10^{-5}$	10^{-4}	$5 \cdot 10^{-4}$
Shape, normalized	10^{-4}	$5 \cdot 10^{-4}$	0.001	$5 \cdot 10^{-5}$	10^{-4}	$5 \cdot 10^{-4}$
Resolution, not normalized	$5 \cdot 10^{-5}$	$5 \cdot 10^{-5}$	10^{-4}	10^{-12}	10^{-12}	$5 \cdot 10^{-6}$
Resolution, normalized	$5 \cdot 10^{-5}$	10^{-4}	$5 \cdot 10^{-4}$	10^{-12}	10^{-10}	$5 \cdot 10^{-6}$

Table A.1: Regularization parameter α of L^2-Regularization leading to highest values of image quality measures.

Step Size	$PSNR_{max}$			$SSIM_{max}$		
Data	$\tau = 0$	$\tau = 1$	$\tau = 5$	$\tau = 0$	$\tau = 1$	$\tau = 5$
Shape, not normalized	0.001	10^{-4}	0.01	0.001	10^{-4}	0.01
Shape, normalized	10^{-4}	0.01	0.001	10^{-4}	0.01	0.001
Resolution, not normalized	10^{-4}	10^{-4}	10^{-4}	10^{-4}	10^{-4}	10^{-4}
Resolution, normalized	10^{-4}	0.01	0.001	10^{-4}	10^{-4}	0.001

Table A.2: Step size of the DIP method leading to highest values of image quality measures.

Iteration	$PSNR_{max}$			$SSIM_{max}$		
Data	$\tau = 0$	$\tau = 1$	$\tau = 5$	$\tau = 0$	$\tau = 1$	$\tau = 5$
Shape, not normalized	217	295	320	275	374	359
Shape, normalized	233	416	303	494	416	303
Resolution, not normalized	3932	2737	2307	3982	3586	3902
Resolution, normalized	3351	5	4020	4118	4	3551

Table A.3: Number of iteration of the DIP method leading to highest values of image quality measures.

α_{start}	PSNR_{max}			SSIM_{max}		
Data	$\tau = 0$	$\tau = 1$	$\tau = 5$	$\tau = 0$	$\tau = 1$	$\tau = 5$
Shape, not normalized	10^{-5}	10^{-5}	10^{-4}	10^{-5}	10^{-5}	10^{-4}
Shape, normalized	10^{-5}	10^{-5}	10^{-4}	10^{-5}	10^{-5}	10^{-4}
Resolution, not normalized	10^{-5}	10^{-5}	0.01	10^{-5}	10^{-5}	10^{-5}
Resolution, normalized	10^{-5}	0.01	0.01	10^{-5}	10^{-5}	10^{-5}

Table A.4: Hyperparameter α_{start} of the PnP method leading to highest values of image quality measures.

α_{incr}	PSNR_{max}			SSIM_{max}		
Data	$\tau = 0$	$\tau = 1$	$\tau = 5$	$\tau = 0$	$\tau = 1$	$\tau = 5$
Shape, not normalized	10^{-5}	0.001	0.001	0.001	0.001	10^{-4}
Shape, normalized	10^{-5}	0.001	0.001	10^{-5}	0.001	10^{-4}
Resolution, not normalized	0.001	0.001	10^{-5}	10^{-5}	10^{-5}	10^{-5}
Resolution, normalized	0.001	0.001	0.001	10^{-5}	10^{-5}	10^{-5}

Table A.5: Hyperparameter α_{incr} of the PnP method leading to highest values of image quality measures.

$\lambda\sigma^2$	PSNR_{max}			SSIM_{max}		
Data	$\tau = 0$	$\tau = 1$	$\tau = 5$	$\tau = 0$	$\tau = 1$	$\tau = 5$
Shape, not normalized	10^{-6}	10^{-6}	10^{-6}	10^{-6}	10^{-6}	10^{-6}
Shape, normalized	10^{-6}	10^{-6}	10^{-6}	10^{-6}	10^{-6}	10^{-6}
Resolution, not normalized	10^{-6}	10^{-6}	10^{-6}	10^{-7}	10^{-7}	10^{-7}
Resolution, normalized	10^{-6}	10^{-6}	10^{-6}	10^{-7}	10^{-7}	10^{-7}

Table A.6: Hyperparameter $\lambda\sigma^2$ of the PnP method leading to highest values of image quality measures.

BIBLIOGRAPHY

[Ask+22] Baris Askin, Alper Güngör, Damla Alptekin Soydan, Emine Ulku Saritas, Can Barış Top, and Tolga Cukur. "PP-MPI: A Deep Plug-and-Play Prior for Magnetic Particle Imaging Reconstruction." In: *Machine Learning for Medical Image Reconstruction*. Ed. by Nandinee Haq, Patricia Johnson, Andreas Maier, Chen Qin, Tobias Würfl, and Jaejun Yoo. Vol. 13587. Lecture Notes in Computer Science. Cham: Springer International Publishing, 2022, pp. 105–114. ISBN: 978-3-031-17246-5. DOI: 10.1007/978-3-031-17247-2_11.

[BLS20] Daniel Otero Baguer, Johannes Leuschner, and Maximilian Schmidt. "Computed tomography reconstruction using deep image prior and learned reconstruction methods." In: *Inverse Problems* 36.9 (2020), p. 094004. ISSN: 0266-5611. DOI: 10.1088/1361-6420/aba415.

[Bie12] Sven Biederer. "Superparamagnetische Eisenoxid-Nanopartikel." In: *Magnet-Partikel-Spektrometer*. Ed. by Sven Biederer. Wiesbaden: Vieweg+Teubner Verlag, 2012, pp. 39–63. ISBN: 978-3-8348-2406-6. DOI: 10.1007/978-3-8348-2407-3_3.

[Bru20] Bruker. *Magnetic Particle Imaging: MPI - Bruker's Revolutionary Modality for Preclinical Imaging*. Ed. by Bruker. 2020. URL: https://www.bruker.com/de/products-and-solutions/preclinical-imaging/mpi.html.

[CR04] Daniela Calvetti and Lothar Reichel. "Tikhonov Regularization with a Solution Constraint." In: *SIAM Journal on Scientific Computing* 26.1 (2004), pp. 224–239. ISSN: 1064-8275. DOI: 10.1137/S1064827502412280.

[Dem87] James Weldon Demmel. "On condition numbers and the distance to the nearest ill-posed problem." In: *Numerische Mathematik* 51.3 (1987), pp. 251–289. ISSN: 0029-599X. DOI: 10.1007/BF01400115.

[Dit+] Sören Dittmer, Tobias Kluth, Mads Thorstein Roar Henriksen, and Peter Maass. *Deep image prior for 3D magnetic particle imaging: A quantitative comparison of regularization techniques on Open MPI dataset*. URL: https://arxiv.org/pdf/2007.01593.

[GMHAHE20] Victor Gayoso Martinez, Fernando Hernandez-Alvarez, and Luis Hernandez Encinas. "An Improved Bytewise Approximate Matching Algorithm Suitable for Files of Dissimilar

Sizes." In: *Mathematics* 8 (Apr. 2020), p. 503. DOI: 10.3390/math8040503.

[Ger21] Daniel Gerth. "A new interpretation of (Tikhonov) regularization." In: *Inverse Problems* 37.6 (2021), p. 064002. ISSN: 0266-5611. DOI: 10.1088/1361-6420/abfb4d.

[Gla+20] Anselm von Gladiss, Matthias Graeser, André Behrends, Xin Chen, and Thorsten M. Buzug. "Efficient hybrid 3D system calibration for magnetic particle imaging systems using a dedicated device." In: *Scientific reports* 10.1 (2020), p. 18432. DOI: 10.1038/s41598-020-75122-5.

[GW05] Bernhard Gleich and Jürgen Weizenecker. "Tomographic imaging using the nonlinear response of magnetic particles." In: *Nature* 435.7046 (2005), pp. 1214–1217. DOI: 10.1038/nature03808.

[Häg+12] J. Hägele, F. M. Vogt, J. Barkhausen, T. M. Buzug, and K. Luedtke-Buzug. "Eisenoxidnanopartikel für Magnetic Particle Imaging (MPI)." In: *RöFo - Fortschritte auf dem Gebiet der Röntgenstrahlen und der bildgebenden Verfahren* 184.S 01 (2012). ISSN: 1438-9029. DOI: 10.1055/s-0032-1311011.

[He+16] Kaiming He, Xiangyu Zhang, Shaoqing Ren, and Jian Sun. "Deep Residual Learning for Image Recognition." In: *29th IEEE Conference on Computer Vision and Pattern Recognition*. Piscataway, NJ: IEEE, 2016, pp. 770–778. ISBN: 978-1-4673-8851-1. DOI: 10.1109/CVPR.2016.90.

[HZ10] Alain Hore and Djemel Ziou. "Image Quality Metrics: PSNR vs. SSIM." In: *2010 20th International Conference on Pattern Recognition (ICPR 2010)*. Piscataway, NJ: IEEE, 2010, pp. 2366–2369. ISBN: 978-1-4244-7542-1. DOI: 10.1109/ICPR.2010.579.

[KJ19] Tobias Kluth and Bangti Jin. "Enhanced reconstruction in magnetic particle imaging by whitening and randomized SVD approximation." In: *Physics in medicine and biology* 64.12 (2019), p. 125026. ISSN: 0031-9155. DOI: 10.1088/1361-6560/ab1a4f.

[KJ20] Tobias Kluth and Bangti Jin. "L1 data fitting for robust reconstruction in magnetic particle imaging: quantitative evaluation on Open MPI dataset: International Journal on Magnetic Particle Imaging, Vol 6 No 2 (2020)." In: (2020). DOI: 10.18416/IJMPI.2020.2012001.

[KJL18] Tobias Kluth, Bangti Jin, and Guanglian Li. "On the degree of ill-posedness of multi-dimensional magnetic particle imaging." In: *Inverse Problems* 34.9 (2018), p. 095006. ISSN: 0266-5611. DOI: 10.1088/1361-6420/aad015.

[Kno+18] T. Knopp, T. Viereck, G. Bringout, M. Ahlborg, A. von Gladiss, C. Kaethner, A. Neumann, P. Vogel, J. Rahmer, and M. Möddel. "MDF: Magnetic Particle Imaging Data Format." In: *ArXiv e-prints* (Jan. 2018). arXiv: 1602.06072v6 [physics.med-ph].

[Kno11] Tobias Knopp. "Effiziente Rekonstruktion und alternative Spulentopologien für Magnetic-Particle-Imaging." In: *Ausgezeichnete Informatikdissertationen 2010*. Ed. by Steffen Hölldobler and et al. Bonn: Gesellschaft für Informatik, 2011, pp. 151–160.

[Kno+10a] Tobias Knopp, Sven Biederer, Time F. Sattel, Jürgen Rahmer, Jürgen Weizenecker, Bernhard Gleich, Jörn Borgert, and Thorsten M. Buzug. "2D model-based reconstruction for magnetic particle imaging." In: *Medical physics* 37.2 (2010), pp. 485–491. ISSN: 0094-2405. DOI: 10.1118/1.3271258.

[KJG23] Tobias Knopp, Paul Jürß, and Mirco Grosser. "A Deep Learning Approach for Automatic Image Reconstruction in MPI: International Journal on Magnetic Particle Imaging IJMPI, Vol 9 No 1 Suppl 1 (2023)." In: (2023). DOI: 10.18416/IJMPI.2023.2303008.

[Kno+10b] Tobias Knopp, Timo F. Sattel, Sven Biederer, Jürgen Rahmer, Jürgen Weizenecker, Bernhard Gleich, Jörn Borgert, and Thorsten M. Buzug. "Model-based reconstruction for magnetic particle imaging." In: *IEEE transactions on medical imaging* 29.1 (2010), pp. 12–18. DOI: 10.1109/TMI.2009.2021612.

[Kno+20] Tobias Knopp, Patryk Szwargulski, Florian Griese, and Matthias Gräser. "OpenMPIData: An initiative for freely accessible magnetic particle imaging data." In: *Data in brief* 28 (2020), p. 104971. DOI: 10.1016/j.dib.2019.104971.

[Kri12] Alex Krizhevsky. "Learning Multiple Layers of Features from Tiny Images." In: *University of Toronto* (May 2012).

[Le+23] Tuan-Anh Le, Minh Phu Bui, Khaled Mohamed Gadelmowla, Seungjun Oh, and Jungwon Yoon. "First Human-scale Magnetic Particle Imaging System with Superconductor: International Journal on Magnetic Particle Imaging IJMPI, Vol 9 No 1 Suppl 1 (2023)." In: (2023). DOI: 10.18416/IJMPI.2023.2303032.

[MW] Thomas März and Andreas Weinmann. *Model-Based Reconstruction for Magnetic Particle Imaging in 2D and 3D*. URL: https://arxiv.org/pdf/1605.08095.

[NK23] Alexander Neumann and Tobias Klemme. "System-matrix based reconstruction in magnetic particle imaging: International Journal on Magnetic Particle Imaging IJMPI, Vol 9 No 1 Suppl 1 (2023)." In: (2023). DOI: 10.18416/IJMPI.2023.2303005.

[Pay+20] Hendrik Paysen, Olaf Kosch, James Wells, Norbert Loewa, and Frank Wiekhorst. "Characterization of noise and background signals in a magnetic particle imaging system." In: *Physics in medicine and biology* 65.23 (2020). ISSN: 0031-9155. DOI: 10.1088/1361-6560/abc364.

[PTH23] Huiling Peng, Jie Tian, and Hui Hui. "Self-supervised signal denoising in magnetic particle imaging: International Journal on Magnetic Particle Imaging IJMPI, Vol 9 No 1 Suppl 1 (2023)." In: (2023). DOI: 10.18416/IJMPI.2023.2303039.

[Rah+15] J. Rahmer, A. Halkola, B. Gleich, I. Schmale, and J. Borgert. "First experimental evidence of the feasibility of multi-color magnetic particle imaging." In: *Physics in medicine and biology* 60.5 (2015), pp. 1775–1791. ISSN: 0031-9155. DOI: 10.1088/0031-9155/60/5/1775.

[RFB] Olaf Ronneberger, Philipp Fischer, and Thomas Brox. *U-Net: Convolutional Networks for Biomedical Image Segmentation*. URL: http://arxiv.org/pdf/1505.04597v1.

[Sar+13] Emine U. Saritas, Patrick W. Goodwill, Laura R. Croft, Justin J. Konkle, Kuan Lu, Bo Zheng, and Steven M. Conolly. "Magnetic particle imaging (MPI) for NMR and MRI researchers." In: *Journal of magnetic resonance (San Diego, Calif. : 1997)* 229 (2013), pp. 116–126. DOI: 10.1016/j.jmr.2012.11.029.

[Sha+22] Yaxin Shang, Jie Liu, Liwen Zhang, Xiangjun Wu, Peng Zhang, Lin Yin, Hui Hui, and Jie Tian. "Deep learning for improving the spatial resolution of magnetic particle imaging." In: *Physics in medicine and biology* 67.12 (2022). ISSN: 0031-9155. DOI: 10.1088/1361-6560/ac6e24.

[Tal+20] Nazanin Talebloo, Mithil Gudi, Neil Robertson, and Ping Wang. "Magnetic Particle Imaging: Current Applications in Biomedical Research." In: *Journal of magnetic resonance imaging : JMRI* 51.6 (2020), pp. 1659–1668. DOI: 10.1002/jmri.26875.

[TSH03] M. Taupitz, S. Schmitz, and B. Hamm. "Superparamagnetische Eisenoxidpartikel: Aktueller Stand und zukünftige Entwicklungen." In: *RöFo - Fortschritte auf dem Gebiet der Röntgenstrahlen und der bildgebenden Verfahren* 175.6 (2003), pp. 752–765. ISSN: 1438-9029. DOI: 10.1055/s-2003-39935.

[TA77] Andrey N. Tikhonov and Vasiliy Y. Arsenin. *Solutions of ill-posed problems*. Washington, D.C.: John Wiley & Sons, New York: V. H. Winston & Sons, 1977.

[TG20] Can Baris Top and Alper Gungor. "Tomographic Field Free Line Magnetic Particle Imaging With an Open-Sided Scanner Configuration." In: *IEEE transactions on medical imaging* 39.12 (2020), pp. 4164–4173. DOI: 10.1109/TMI.2020.3014197.

[UVL20] Dmitry Ulyanov, Andrea Vedaldi, and Victor Lempitsky. *Deep Image Prior*. 2020. DOI: 10.1007/s11263-020-01303-4. URL: https://arxiv.org/pdf/1711.10925.

[VBW13] Singanallur V. Venkatakrishnan, Charles A. Bouman, and Brendt Wohlberg. "Plug-and-Play priors for model based reconstruction." In: *2013 IEEE Global Conference on Signal and Information Processing*. IEEE, 2013, pp. 945–948. ISBN: 978-1-4799-0248-4. DOI: 10.1109/GlobalSIP.2013.6737048.

[Vog+19] Patrick Vogel et al. "Magnetic Particle Imaging meets Computed Tomography: first simultaneous imaging." In: *Scientific reports* 9.1 (2019), p. 12627. DOI: 10.1038/s41598-019-48960-1.

[WA12] Wahajuddin and Sumit Arora. "Superparamagnetic iron oxide nanoparticles: magnetic nanoplatforms as drug carriers." In: *International journal of nanomedicine* 7 (2012), pp. 3445–3471. DOI: 10.2147/IJN.S30320.

[Wei+09] J. Weizenecker, B. Gleich, J. Rahmer, H. Dahnke, and J. Borgert. "Three-dimensional real-time in vivo magnetic particle imaging." In: *Physics in medicine and biology* 54.5 (2009), pp. L1–L10. ISSN: 0031-9155. DOI: 10.1088/0031-9155/54/5/L01.

[WGB08] Juergen Weizenecker, Bernhard Gleich, and Joern Borgert. "Magnetic particle imaging using a field free line." In: *Journal of Physics D: Applied Physics* 41.10 (2008), p. 105009. ISSN: 0022-3727. DOI: 10.1088/0022-3727/41/10/105009.

[Wu+19] L. C. Wu et al. "A Review of Magnetic Particle Imaging and Perspectives on Neuroimaging." In: *AJNR. American journal of neuroradiology* 40.2 (2019), pp. 206–212. DOI: 10.3174/ajnr.A5896.

[Yoo+] Jaejun Yoo, Kyong Hwan Jin, Harshit Gupta, Jerome Yerly, Matthias Stuber, and Michael Unser. *Time-Dependent Deep Image Prior for Dynamic MRI*. URL: https://arxiv.org/pdf/1910.01684.

[Zha+23a] Hui Zhang, jing zhao, Yusong Shen, and Jie Tian. "Deep Generative Adversarial Networks for Direct Super-resolution Magnetic Particle Imaging Reconstruction: International Journal on Magnetic Particle Imaging IJMPI, Vol 9 No 1 Suppl 1 (2023)." In: (2023). DOI: 10.18416/IJMPI.2023.2303011.

[Zha+] Kai Zhang, Yawei Li, Wangmeng Zuo, Lei Zhang, Luc van Gool, and Radu Timofte. *Plug-and-Play Image Restoration with Deep Denoiser Prior*. URL: http://arxiv.org/pdf/2008.13751v2.

[Zha+23b] Peng Zhang, Jie Liu, YiMeng Li, Hui Hui, and Jie Tian. "Multi-color Kaczmarz Method for Color Magnetic Particle Imaging: International Journal on Magnetic Particle Imaging IJMPI, Vol 9 No 1 Suppl 1 (2023)." In: (2023). DOI: 10.18416/IJMPI.2023.2303026.